Influence of cross-section on the aeolian tone: a numerical study in the laminar regime

Wagner J. G. S. Pinto*, Florent Margnat† and Yves Gervais ‡
Institut Pprime, Département Fluides, Thermique, Combustion - Université de Poitiers, ISAE-ENSMA, CNRS - Bât. B17
6 rue Marcel Doré TSA 41105, 86073, Poitiers Cedex 9, France

Influence of the cross section on airframe noise is investigated numerically in 2D at low Reynolds number (Re = 150**) by a direct Navier-Stokes (DNS) solver and an acoustic power formulation derived from an hybrid acoustic analogy. Flows around different canonical geometries (rectangle, triangle, ellipse and lozenge) and of different breadth-to-height ratio, called as aspect ratio (**AR**), are studied. The appearance of a wake organization with two rows of vortices is associated with a peak of RMS lift and frequency. Several relationships between flow integral, geometrical and topological quantities are proposed and discussed. The hormetic response of the RMS lift coefficient to the increase of** AR **is noticed for all geometries. The RMS lift coefficient, thus the noise, is found to correlate linearly to the vortex displacement normal to the flow and to the fourth power of the average drag.**

I. Introduction

Numerical and experimental investigations about aeolian tone and bluff-body aerodynamics are largely present in the literature. Despite the tremendous advances those works have yielded, the comprehension of the main aspects on how the geometry influences the flow and the noise production, as urged by Roshko [1], remains unclear and a closed model is still unavailable.

This analysis is performed with the idea that focus should be given not only to controlling the phenomena (with porous coats, jets, etc), that are currently being adapted to real engineering applications, but also on the basis of the mechanism behind the vortex shedding in order to decrypt the influence of the shape of the body. Within that aim, the design can be more conscious about the aerodynamic and aeroacoustical traits of a flow and both aspects will be better integrated to the development stages of engineering products.

Since the canonical works of Roshko [2, 3], other articles must be cited in what concerns the shape influence in bluff-body aerodynamics. Flow dependency to cross section at low Reynolds number ($\mathrm{Re} < 1,000$) has been discussed by Cheng & Liu [4], who highlighted the importance of the separation of the shear layers in the definition of the wake. Flow and sound emission of rectangles of different width-to-height ratios (referenced as aspect ratio - AR - on this document) and angles of attack have been studied by Inasawa [5] and Margnat [6], who discussed the change of wake topology and the shift of the dipole downstream with increase of the AR.

For high Reynolds number ($\mathrm{Re} > 1,000$), one shall cite the experimental study of the effect of incidence and afterbody shape by Luo et al. [7], who also emphasized the importance of shape in defining the shear layers distance, thus, the wake organization. Hu & Zhou [8] have experimentally evaluated the link between several flow quantities. More aeroacoutics oriented works are also available, such as the paper by Becker et al. [9] who associated the wall-mounted cylinders cross-section to the noise by its enhancement of flow two-dimensionality and of the influence on roof vortex. Last but not least, the studies of the sound emission of different elliptical and rectangular sections by King & Pfizenmaier [10] and Iglesias et al.[11], both emphasizing the importance of the aspect ratio in the sound emission.

Current study is based on 2D, low Reynolds number (Re = 150) simulations for canonical bodies of different aspect ratios. The benefit of performing an analysis in the laminar regime resides in the low computational cost, what allows a relatively fast flow computation with a high-fidelity solver without any turbulence modeling. In the same spirit, a simplified formulation based on Curle's analogy [12] is used for the quantification of the sound emission. Rather than performing a detail description of the acoustical and aerodynamical fields generated by a single or few geometries, the current approach is based on the construction of a database of results and later a statistical analysis.

*PhD student, Fluids, Thermal and Combustion Sciences Department, wagner.goncalves@univ-poitiers.fr.
†Assistant Professor, florent.margnat@univ-poitiers.fr
‡Professor, yves.gervais@univ-poitiers.fr

The number of observations in this works remains in between the few cases of a typical CFD study and the hundreds to thousands of observations that compose statistical studies. To be compatible to the available resources, the objective is not to propose a closed model of the aeolian tone generation, but rather to confirm and emphasize relationships that are independent of the geometry and to try to quantify the ones that have shape dependency, providing physical insights about the phenomenon. Since this application is aimed at airframe noise, focus is given to unsteady properties, fundamentally the fluctuating force coefficients, which are the major ingredients of the obstacle noise [13, 14].

The use of low Reynolds number simulations reduces drastically the direct application of the current results and observations to real engineering applications. However, the discussion presented here is focused on the basis of the Von-Karman vortex shedding, a phenomenon that is still present in a large range of flow regimes. In a practical point of view, current results can be applied for either increasing (for energy harvesting or even music production) or reducing (noise and structural stress mitigation) the fluctuating lift.

The document is organized as follows. Section II contains the description of the solver, numerical setup, aeroacoustical analogy and the tested shapes, respectively. Obtained flows are discussed in terms of integral quantities and topology in Section III, with the definition of the recirculation and formation length and the parameter that quantifies the distance to the onset of unsteadiness. Section IV presents the empirical relations that are derived from the produced database, firstly for topology based variables (IV.A) and secondly for models that use integral quantities (IV.B). A synthesis of the results with a final discussion and conclusions are presented in Section V. Graphs with the validation and samples of regression laws applied to every geometry individually are available in the appendix.

Since major part of the laws are power or exponential, most graphs are shown in both linear and logarithm scales.

II. Methodology

The flow is analyzed numerically in two dimensions (2D). A hybrid aeroacoustical approach is employed, based on Curle's [12] derivation from the Lighthill formulation [15]. The two steps, as well as the tested geometries, are presented next.

A. Numerical solver

The aerodynamic simulations are performed using a finite differences direct Navier-Stokes (DNS) incompressible solver [16]. Space derivatives are calculated using a compact, centered scheme of order 6, and temporal marching is performed using a 3rd order Runge-Kutta formulation. The pressure field, allocated in a staggered grid, is solved in the spectral domain in a sub-step that guarantees the flow incompressibility. An Immersed Boundary Method (IBM) with a forcing term [17] is used for imposing the no-slip condition at the geometry boundary, leading to the following momentum equation:

$$\begin{aligned} \frac{\partial u_i}{\partial t} + u_j \frac{\partial u_i}{\partial x_j} &= -\frac{\partial}{\partial x_j}[p\delta_{ij} - \tau_{ij}] + F_i \\ \mathbf{F}(\mathbf{x},t) &= -\epsilon(\mathbf{x}) \left[\omega_n^2 \int_0^t \mathbf{u}(\mathbf{x},t)dt + 2\zeta\omega_n \mathbf{u}(\mathbf{x},t) \right] \end{aligned} \tag{1}$$

where $\mathbf{u}$ is the velocity vector, $\mathbf{x}$ is the position, p is the pressure, δ_{ij} is the Kronecker delta, τ_{ij} are the shear stress tensor components, $\mathbf{F}$ is the IBM forcing term, $\epsilon(\mathbf{x})$ is a matrix that defines the solid and fluid domains, $\omega_n = 50$ and $\zeta = 1$ [17] are the IBM coefficients. Elements in the $\epsilon(\mathbf{x})$ array are defined as 1 if the node is inside the ideal contour of the shape that is simulated (solid domain), 0 elsewhere (fluid domain).

Naturally, the use of an IBM solver has the drawback of the nonexistent description of wall quantities, specially in the current form where there is no imposition in order to adapt the wall discontinuities. At low Reynolds number such geometrical details have diminutive influence in the final result and the use of such strategy allows the production of multiple geometries without the need to remesh.

The domain is $25.3d$ long and $20d$ wide, where d is the height of the obstacle. The geometry center, taken as the origin of the coordinate system, is placed at a streamwise distance of $11d$ from the inlet and at the lateral center of the domain ($10d$ from the boundaries), the discretization is of 649×257 elements, mesh stretched in y. Once the geometries are represented via a virtual boundary methodology with no interpolation to impose the shape, geometrical features are limited in precision (there are approximately 25 elements per d in the streamwise direction). Performed convergence tests for mesh, time and size of the domain are detailed in [18, 19]; validation is available on appendix

V.A. Boundary conditions are set as follows: uniform velocity on the inlet; convective condition at the outlet; and slip condition at the lateral walls. This numerical setup is presented in Fig. 1.

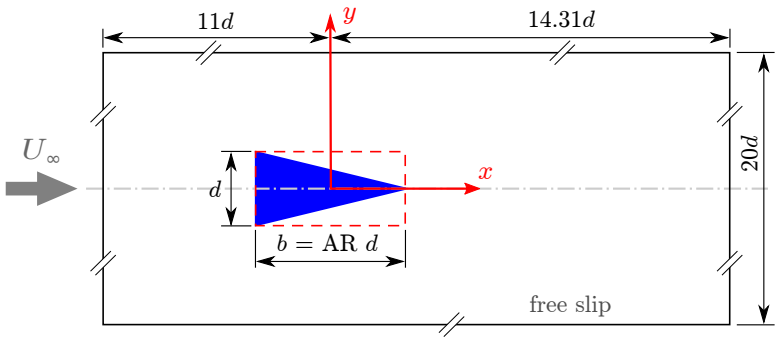

Fig. 1 Numerical setup. The coordinate system is placed at the center of the obstacle.

The wake period is defined as the interval between two lift peaks, what also defines the vortex shedding frequency f. The Strouhal and Reynolds numbers consider the sectional height d as the reference dimension (constant for all tested shapes):

$$\mathrm{St} = \frac{f d}{U_\infty} \qquad \mathrm{Re} = \frac{U_\infty d}{\nu} \tag{2}$$

where ν is the kinematic viscosity. The present analysis is focused on the solutions at Re = 150, although some of the results are also based in simulations performed at even lower Reynolds numbers.

Integral description of the flow is based on the force coefficients:

$$C_D = \frac{D}{\frac{1}{2}\rho U_\infty^2 d} \qquad C_L = \frac{L}{\frac{1}{2}\rho U_\infty^2 d} \tag{3}$$

where D is the drag, L is the lift, ρ is the density in the propagation medium and U_∞ is the upstream velocity. Since the shapes studied in this work are symmetrical, the average C_L is null. C'_D and C'_L are the period's root mean square (RMS) of the fluctuation of drag and lift coefficients.

B. Acoustical analogy

The acoustic power of each shape is estimated using a model based on Curle's analogy for the tonal component of a compact source. A single formula [6] is employed:

$$W = \frac{\pi}{16}\rho U_\infty^3 d\ \mathrm{St}\ \mathrm{M}^2(2{C'_D}^2 + {C'_L}^2) \tag{4}$$

where W is the acoustic power (integral of the acoustic intensity over an observer circle of arbitrary radius in the far field). Noting c the sound velocity, $\mathrm{M} = U_\infty/c$ is the Mach number. Since simulations are incompressible the Mach number is undefined. In order to scale the results, a value of M = 0.1 is considered. Since $\rho U_\infty^3 d$ represents the reference power (by unit length) supplied by the incoming flow and is constant in all current simulations, the non-dimensional acoustical power W_a, herein also referred to as acoustic efficiency, is considered:

$$W_a = \frac{W}{\rho U_\infty^3 d} = \frac{\pi}{16}\mathrm{St}\mathrm{M}^2(2{C'_D}^2 + {C'_L}^2) \tag{5}$$

C. Tested geometries

In order to investigate the shape influence on aeolian tone, several cross-sections of fixed height d are simulated (see Fig. 2, noting that the half ellipsoids are not included in the totality of this study). Besides the construction paradigm, the sectional breadth b, condensed in the non-dimensional parameter aspect ratio $\mathrm{AR} = b/d$, is also modified. In total, 104 cases (combination of geometry and aspect ratio) are simulated. The model shown in Fig. 2 is trib for AR = 2.0.

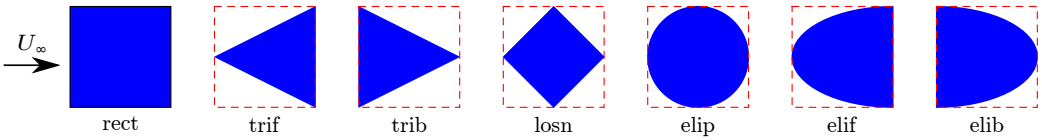

Fig. 2 Set of tested geometries, at unitary aspect ratio, from left to right: rectangle (rect), front-pointing triangle (trif) and back-pointing triangle (trib), lozengle (losn), ellipse (elip), front-pointing half ellipse (elif), back-pointing half ellipse (elib).

Note that the use of the geometrical paradigms illustrated in Fig. 2 is an artifice for having several geometries that share common features. That is, each individual case (geometrical paradigm + aspect ratio) is an independent shape by itself, however the fact that only the aspect ratio is modified allows for an analysis based on those subgroups and to check tendencies associated with the breadth of the obstacle. The use of the aspect ratio as the modifier is also motivated by the observations done in previous works that revealed the importance of the length in the tonal sound production [18, 19], phenomenon also present in high Reynolds number (further studied in another work presented at the same conference [20]).

III. Flow description

This section is dedicated to the general description of the flow from integral quantities to topological features, focusing on the differences and similarities that are obtained when modifying the shape and the aspect ratio. Due to the use of an IBM formalism, surface quantities such as the surface pressure, friction coefficient and the viscous share of the aerodynamic efforts are not directly available. Authors are still developing a method for reliable estimations of wall quantities from current IBM implementation, so wall related quantities are not considered in this work.

A. Integral quantities

1. General trends

Figure 3 presents the evolution of integral quantities (average drag coefficient, RMS lift and drag coefficients and Strouhal number) with the aspect ratio. For all the geometries, the response to an increase of AR is similar: a reduction of RMS and average drag coefficients and an rapid increase followed by a peak and a slow decrease of C'_L and St; the change of tendency (from growing to decreasing) noted for the last 2 variables is discussed later in the document (Section III.B).

In terms of noise production, the estimation of the acoustic efficiency provided by Equation 4 and 5 is applied and the results are illustrated in Fig. 4. The considered acoustic analogy based model indicates that $W_a = f(\mathrm{St}, C'^2_D, C'^2_L)$, where all the variables are shape dependent. The relationship between the acoustic efficiency and the square of the lift coefficient fluctuation is as well presented in Fig. 4. The fact that a linear trend is noted indicates that among the 3 terms the C'_L is the major factor in the construction of the tonal noise.

It is observed that the fluctuating lift is the most relevant quantity not only in terms of magnitude but also in its dependency to shape. While the other two parameters (St,C'_D) are only slightly modified when comparing different geometries (Strouhal number values lies in the range of 0.12 to 0.22 and the fluctuating drag is about 1/10 of the fluctuating lift), the C'_L is the quantity that has a more scattered distribution considering the tested geometries. In the same direction, previous optimization studies performed by the authors under the same hypothesis and tonal noise formulation for 2 distinct shape parametrizations [18, 19] found that the geometries that have extreme behavior (minimum or maximum) in terms of acoustic efficiency and RMS lift coefficient are practically the same.

2. Influence of shape

Globally, the elliptical and square sections can be taken as shapes that minimize the average and fluctuating efforts. On the other hand, the back-pointing triangle is the shape that has the biggest drag and the highest RMS lift coefficient. The front-facing triangles are the obstacles with the biggest Strouhal numbers and RMS drag coefficients. The dichotomy between the two triangles is an interesting result that correlates to the concept of "bluffness" introduced by Roshko [3]. When considering the St, those shapes represent the extrema (trif the maximum and trib the minimum). This can be

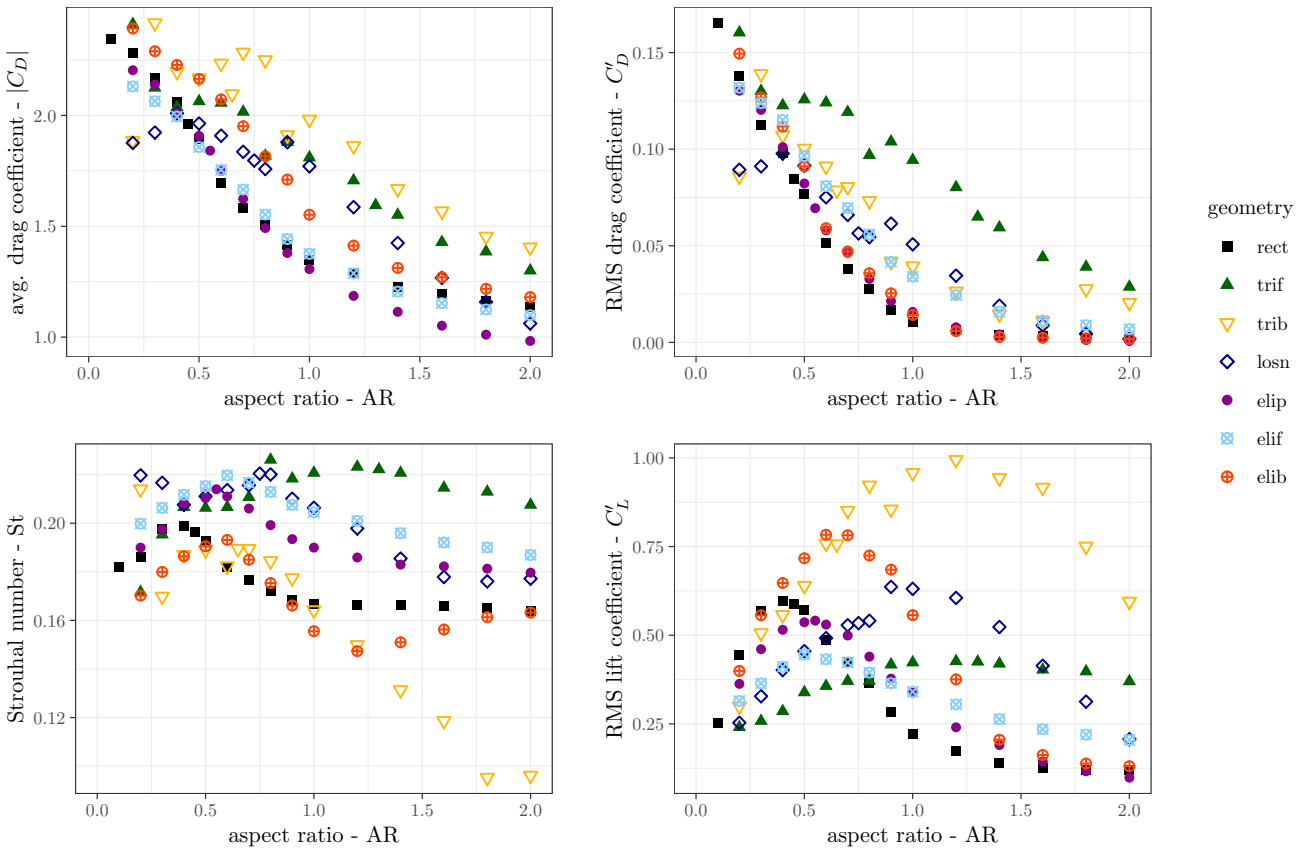

Fig. 3 Evolution of the mean and RMS drag coefficients, Strouhal number and RMS lift coefficient with the aspect ratio for all tested shapes, Re = 150**.**

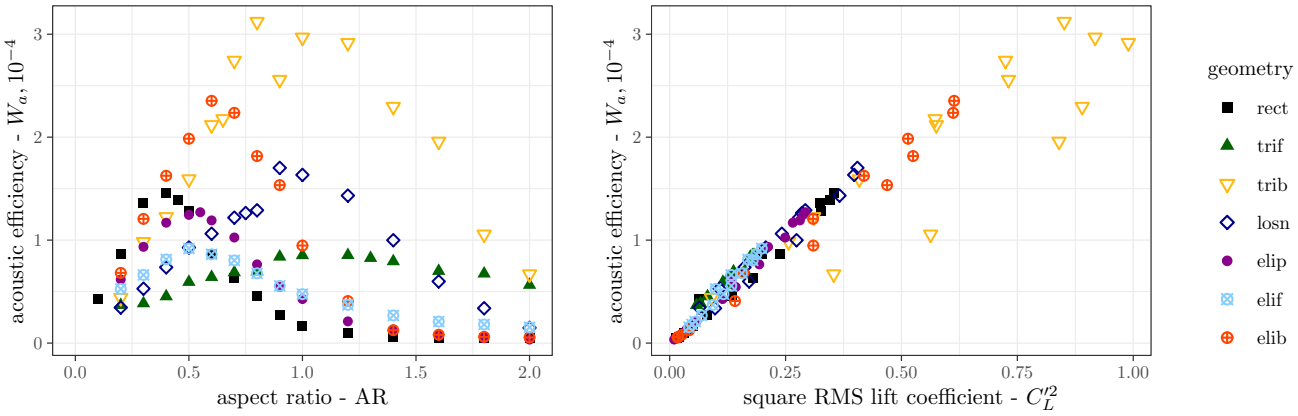

Fig. 4 Evolution of the acoustic efficiency with the aspect ratio (left) and the relationship of the acoustic efficiency and the RMS lift coefficient (right), Re = 150**.**

justified by the difference in the orientation of the lateral boundaries: while for the front-pointing triangle the shear layers are pushed away form each other, the walls of the back-pointing triangle induce to an approximation of those layers. Distant layers correspond to wider wakes, thus, higher Strouhal numbers [3, 21]. Even if not as extreme, same conclusion is noted when comparing the half-elliptical sections elif and elip. More detailing is performed with the

quantification of flow topology features, presented on the section III.B.

B. Flow topology

In terms of flow topology, the typical unsteady Von-Karman wake is present for all the geometries with a periodical vortex shedding. Overall, for the average flow, there is a flow acceleration on the laterals of the body, marked by negative Z-vorticity ($\omega_z = \partial v/\partial x - \partial u/\partial y$) on the top and positive on the bottom; u_x reaches up to 1.5 the inlet velocity and maximum magnitude of u_y is of about 0.5 U_∞; the pressure is elevated at upstream and a base value is encountered in the downstream part of the body where a recirculation region is present in the averaged flow. The described flow is exemplified in Fig. 5, where mean fields of the flow around the square section are presented.

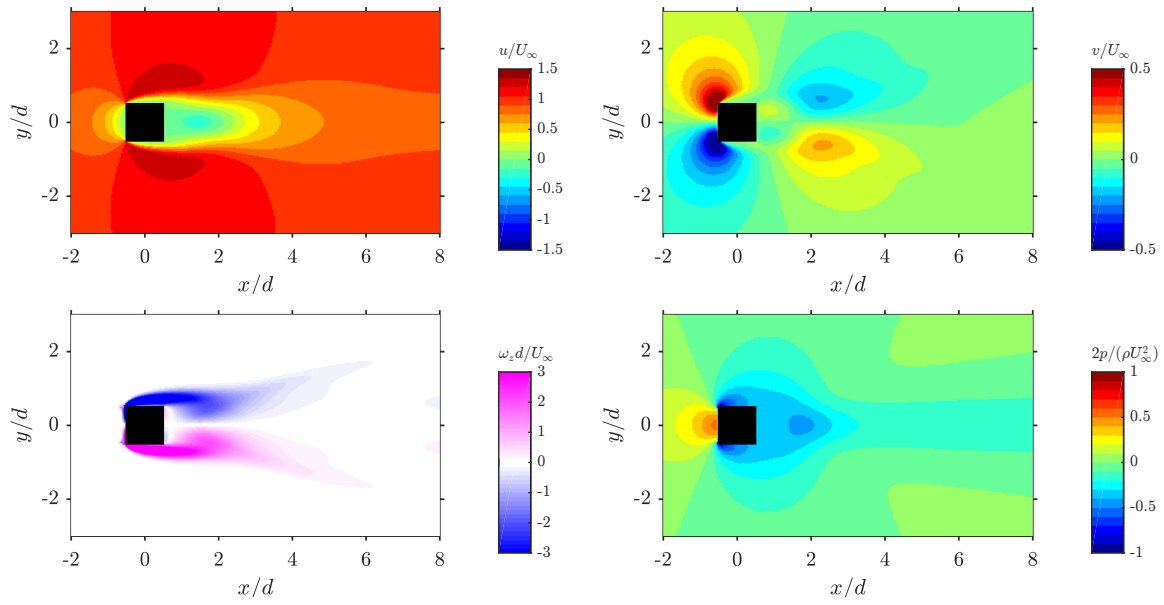

Fig. 5 Mean flow fields for the square section (rect, AR = 1.0**),** Re **= 150.**

In what concerns the far-wake vortices distribution, two regimes are noted and shown in Fig. 6. At regime I, all vortices that are shed are kept aligned an a single row that has its center coincident to the axis of symmetry of the obstacle. For regime II, the initial single row wake transforms into 2 rows of vortices of equal vorticity sign. For all the tested geometries there is a clear distinction between the aspect ratios that provoke each one of those two vortex dispositions, and the change from geometries with initially single and further downstream double (regime II, for "small" AR, generally speaking) to and completely single row (regime I, "big" AR) is associated with the peaks of RMS lift and Strouhal highlighted previously in Section III.A.

Such behavior is also discussed by Johnson et al. [22] and Thompson et al. [23] in their studies of elliptical sections, the work of Saha et al. [24] around flat plates, and the articles of Ng et al. [25] and Mahato et al. [26] describing the flow around triangular sections. In [25], there are actually 5 regimes associated with the modification of the Reynolds number and the angle of attack of the triangle. It has also been noted on the forecited works that the two rows can evolve to a second shedding with a distinct frequency.

As discussed by Johnson et al. [22], the phenomenon is associated to a large Re and/or an small aspect ratio. Thompson et al. [23] associated the x-position of the transition from single to double row to the Reynolds number (transition is pushed upstream with the increase of Re), and also its persistence downstream. Since the streamwise domain used in this work is relatively small ($-11 \leq x/d \leq 14.31$), it is possible that the development into two rows could take place for other geometries that were tested but is simply not noted due to the simulation not capturing that transition. Saha et al. [24] suggests that there are no major modifications in the integral quantities associated with this far-wake structures, thus, the current setup is believed to simulate the flow behavior correctly.

This work allows to imply that the phenomenon is universal in what concerns the shape of the obstacle. The association of that modification of the wake with change in the Reynolds number scale being comparable to a change in the aspect ratio leads to the conclusion that the modification of the geometry, also in the sense of changing the

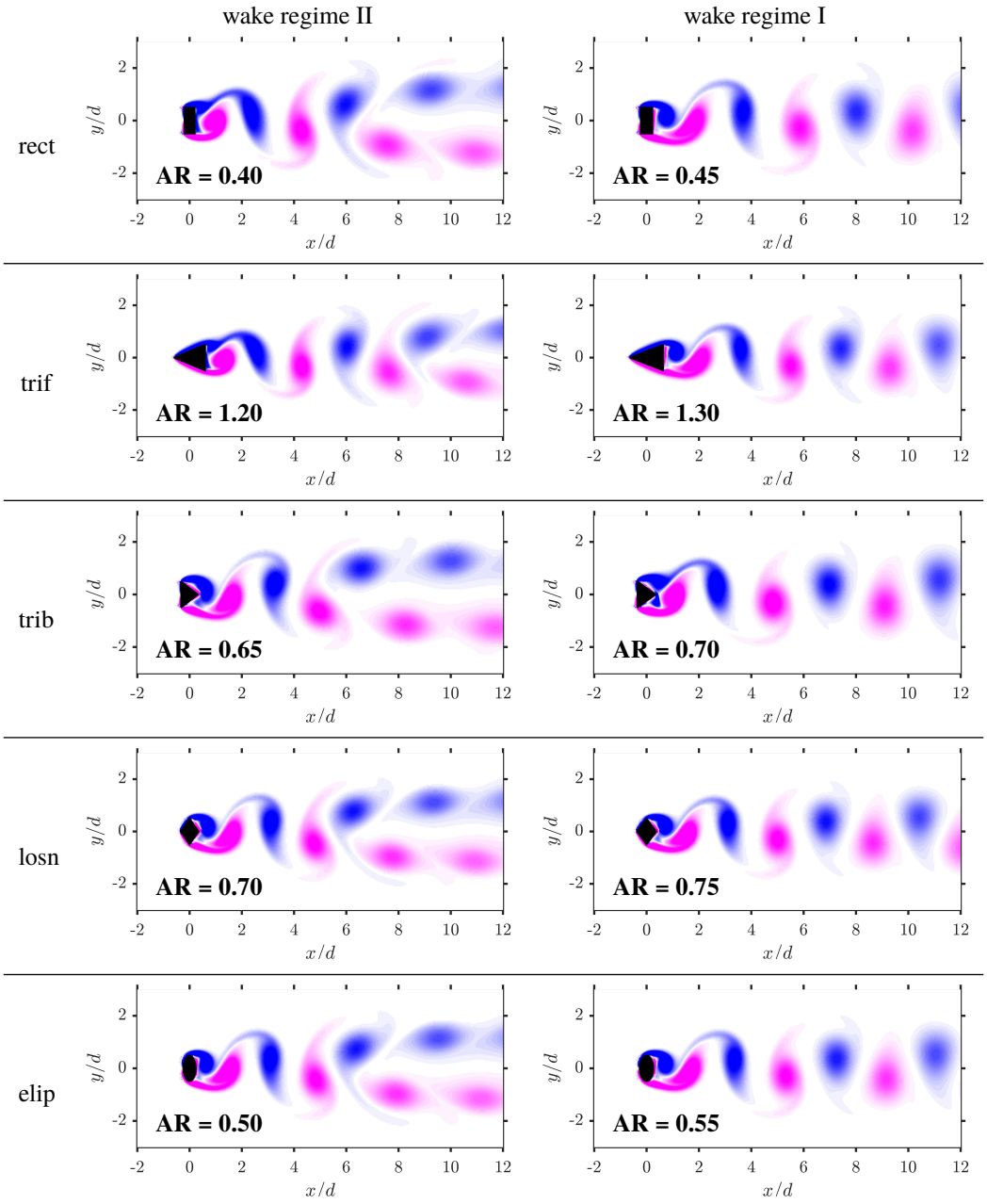

Fig. 6 Instantaneous vorticity contour for the two wake regimes, multiple geometries, Re **= 150. Vorticity scale is of** $[-3\omega_z d/U_\infty, +3\omega_z d/U_\infty]$**, same as in Fig. 5.**

geometrical features, is the same as a modification of the Reynolds number. In that sense, further investigations need to focus on dealing with the quantification of the evolution of the flow, not being exclusively attached to a value of Reynolds number that is reductive of the full extension of the influence of the shape in the flow. A further development of this argument is presented next on Section III.D.

C. Formation length and recirculation length

Two variables are evaluated in order to quantify the flow distribution at the near body wake: the recirculation length L_r, taken as the size of the average flow recirculation bubble in the streamwise direction, and the formation length L_f, a measurement of the distance between the body and the region of maximal flow perturbation that is analogous to the

region where the vortices are shed. The interest in quantifying those values resides in the fact that those parameters are related to the vortex shedding by the characterization of the mean flow topology and the position where the vortices are shed, thus, representative of the noise production mechanism.

There are different definitions present in the literature for the formation length [27]. In this work, it is based on the position of the point where the RMS of the streamwise velocity fluctuation (u') is maximal. The formation length is then defined as the distance between the downstream limit of the body and this position:

$$L_f = x \text{ of } \max(u') - \frac{\text{AR}}{2} \tag{6}$$

Figure 7 presents three examples of recirculation and formation lengths by superposing the u' field and the mean flow streamlines.

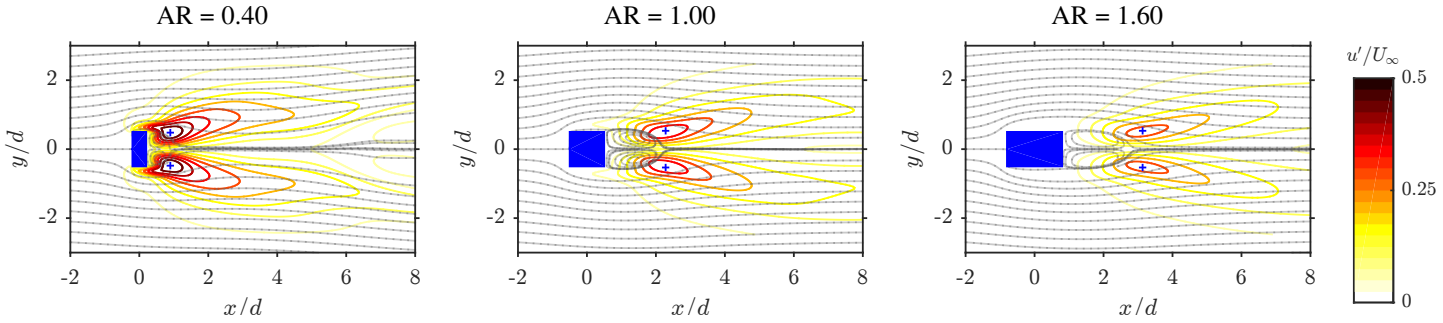

Fig. 7 Field of RMS streamwise velocity (u') superposed by the mean flow streamlines for rectangular sections (rect) of multiple AR**,** Re **= 150. Crosses represent the position of maximum u'.**

As exemplified in Fig. 7, for small AR, the formation length is smaller than L_r. For extended bodies, $L_f > L_r$. The evolution of the two quantities with the aspect ratio is presented in Fig. 8.

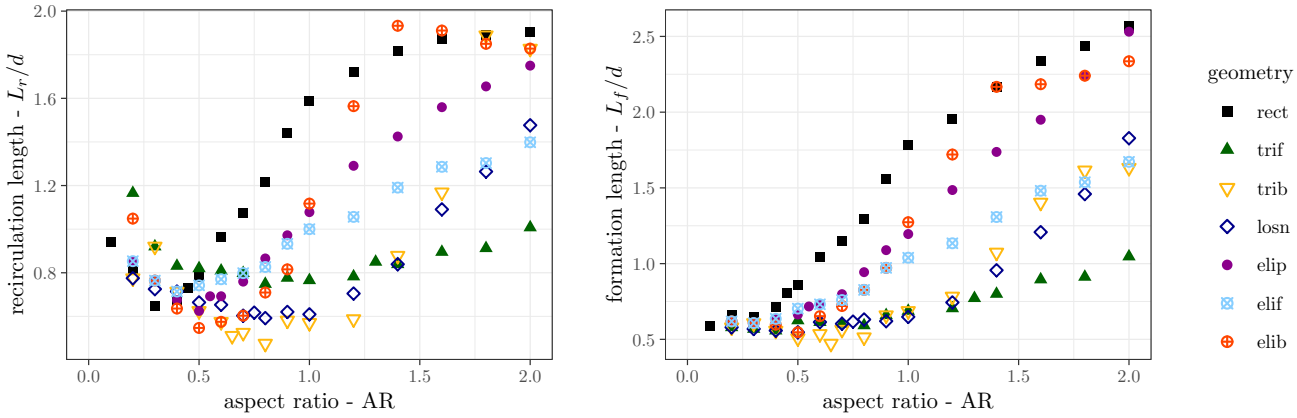

Fig. 8 Evolution of the recirculation length (left) and formation length (right) with the aspect ratio, Re **= 150.**

The formation length presents a monotonic growth with the increase of the aspect ratio. For the recirculation length, from AR = 0.1 to 2.0, there is an initial decrease followed by an increase. For the elliptical section, for example, this change in tendency is observed at AR = 0.55. This is believed to be provoked by non-linearities present in the flow around the shorter sections, as discussed by Pier [28]. It can also be noted that there is a lower limit $\min(L_r) \approx 0.6d$, also present for the formation length $\min(L_f) \approx 0.6$. This behavior is the exact opposite of what is noted in the curves of C'_L and St (Fig. 3) that have peaks, point also present in the article by Inasawa et al. [5].

For longer geometries, both recirculation and formation lengths are elevated, what synthesizes the fact that the longer the geometry, more dissipation takes place at the walls. That means that the wake is less energetic (noted by the reduction of the magnitudes at the RMS velocity fields in Fig. 7), and the flow instability is pushed downstream.

Aiming at a quantification of that energetic state, a discussion about the distance of the flow to the onset of unsteadiness is presented next.

D. Quantification of the distance to the onset of unsteadiness

The change of cross-section shape is fundamentally a modification of how a corresponding excitation is going to take place in the fluid. However, as the body is the origin of that excitation, it is also an alteration of the forcing condition that provokes the flow to behave differently. In this sense, an energetic based parameter must also be considered when comparing flow around different geometries.

Although being intuitive, the relation between the velocity and force fluctuations has not yet been well investigated [29]. One of the strategies to characterize the shape influence on noise is then an analysis based on flow instability principles, once the perturbations in the wake are directly associated with the instability modes for both the frequency and amplitude [28, 30]. Based on the fact that, close to the steady to unsteady flow transition, the velocity fluctuations may be proportional to the corresponding distance to transition, the following parameter is used [30–32]:

$$\varepsilon = \frac{\mathrm{Re} - \mathrm{Re}_c}{\mathrm{Re}_c} \tag{7}$$

where Re_c is the critical Reynolds number.

It is a rather global criteria, representing the distance to the onset of unsteadiness for each shape, being closer to account for the geometrical specificities than the Reynolds number itself. In that sense, ε may be taken as a parameter that quantifies a given flow position in an geometry independent scale, being more associated with an universal change in the flow response mechanism with the increase of flow inertia and less with the response of the flow to the geometry change itself.

In a previous study [33], the authors determined the critical Reynolds number for a subset of the shapes that are studied here (elip, losn, rect, trib and trif), using the same numerical setup and solver. The transition was quantified via a bi-section method that considered the fluctuation of the Y-velocity as the criterion for the flow transition. Results are reproduced here and presented in Fig. 9 along with the ε values.

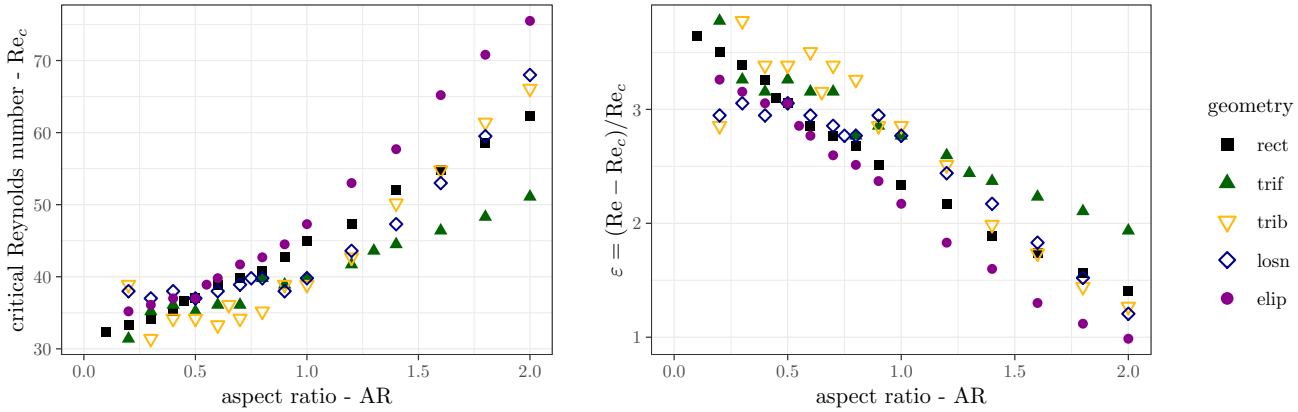

Fig. 9 Evolution of the critical Reynolds number (left) and of ε for Re = 150 (right) with the aspect ratio.

For all tested shapes, there is an exponential increase of the critical Reynolds number with the increase of the sectional breadth [33]. This behavior can be associated with the increase of diffusion of energy at the body instance with the enlargement of the walls, thus, reducing the amount of energy available in the wake at a given Reynolds number, what correlates to the increase of the formation length discussed on previous section. Therefore, the transition is delayed in the Reynolds number scale. Considering the flow at fixed Reynolds number of Re = 150, this represents a decrease of ε with an increase of the aspect ratio.

On Table 1, the aspect ratios corresponding to before and after the apparition of the regime II are presented as well as the corresponding ε for each one of them at Re = 150. This transition takes place at the peaks of Strouhal number and fluctuating lift. It can also be deduced that the second wake regime is observed at $\varepsilon \sim 3$.

Table 1 Properties at the regime transition, Re = 150.

	rect	trif	trib	losn	elip
AR of regime transition	0.40-0.45	1.20-1.30	0.65-0.70	0.70-0.75	0.50-0.55
AR of peak St	0.40	1.20	0.65-0.70*	0.75	0.55
AR of peak C'_L			1.00	0.90	
ε of transition	3.26-3.10	2.60-2.44	3.16-3.39	2.86-2.77	3.05-2.86

*: both AR present the same vortex shedding Strouhal number.

As discussed in [25], the existence of multiple regimes can be actually a sign of transition to a 3D flow. The comparison to literature values indicates that the transition to 3D is around $\varepsilon = 2$, see Table 2.

Table 2 Transition Reynolds number and corresponding ε for 2D to 3D flow transition, AR = 1.0**.**

	references	rect	trif	trib	losn	elip
steady to unsteady transition - Re_c	[33]	45.0	39.8	38.9	39.8	47.3
2D to 3D transition - $Re_{2D\rightarrow 3D}$	[23, 32, 34]	164	100.2	126.3	116	190.3
$\varepsilon_{2D\rightarrow 3D}$		2.64	1.52	2.25	1.91	3.02

Comparison of ε values on Table 1 and 2 together with an extrapolation of the results to all tested aspect ratios induces to the conclusion that the regime II is actually a wake disposition that is only made possible by the absence of the third dimension. In other terms, the fact that the flow cannot dissipate energy in the form of spanwise flow deformation results in the existence of the 2nd Von-Karman instability that may be analogous to the appearance of Mode A in a 3D simulation. This statement is reinforced by the fact that there is a clear distinction between the behavior of the flow quantities when analyzing regimes I and II.

Based on that, most of the current results are presented simultaneously for two groups: regime I only and regime II/all points. Several relations are noted to be spoiled when this aspect is neglected. It is thus recommended that, when analyzing different shapes or flow regimes, to perform individualized analysis based on the flow dynamics, since a modification in the vortex distribution may respect a different law and hide important trends.

IV. Empirical relations

Several relationships between flow quantities and the associated models are presented next. Such results may contribute to the production of bluff-body wake models and yield insights over the physics of the phenomenon. Since this work is concentrated in the study of airframe noise, focus is given to the relation of integral and flow topology quantities to the fluctuating efforts, directly associated with the noise emission.

The choice of the models is mostly defined by what is noted geometrically-wise in detriment of the general relationship. Example of the obtained curves for each geometry are presented on appendix. All linear regression coefficients are obtained using the least-squares formalism.

Section IV.A is dedicated to the laws that correlate the RMS force coefficients to flow quantities, such as the recirculation length. The integral quantities, such as the average drag coefficient, are considered as the explaining variables on section IV.B.

A. Flow topology based relations

This section is dedicated to the relations found between the RMS force coefficients and flow topology quantities: recirculation and formation lengths and ε.

1. RMS lift coefficient vs. recirculation length

Analysis of the curves of the RMS lift coefficient and recirculation length leads to the following linear model:

$$C'_L = \alpha + \beta \frac{L_r}{d} \tag{8}$$

Results are presented in Fig. 10, note that the distinction between the regimes is necessary for this analysis. The fit considering all the geometries is rather poor (determination coefficient of 0.5132 for regime I and 0.5499 for regime II), however, for each geometry, the linear law is very representative of the points (examples in Fig. 22, appendix V.B). An exponential law could be envisaged for fitting the complete data set, but due to the good individual behavior (for each geometry) only the linear model is considered.

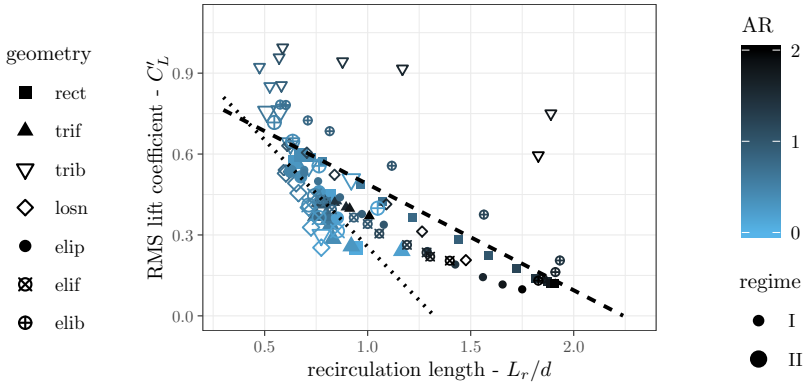

Fig. 10 Evolution of the RMS lift coefficient with the recirculation length, Re = 150**, all geometries, colored by the aspect ratio. Represented regression laws: obtained for regime I (dashed line); and only considering regime II (dotted line).**

Overall, it can be concluded that an increase in the recirculation length is associated with a reduction of the fluctuating lift, also noted by Hu & Zhou [8], and consequently the sound emission. The scattering associated with the shape and the regime implies that both factors are highly influenced by how the average flow is organized. Based on the idea that the distance of the vortices to the lift generating surfaces is a fundamental ingredient in the generation of RMS forces, the relationships between C'_D, C'_L and the formation length are assessed next.

2. RMS force coefficients vs. formation length

The position of the generation of the vortex, synthesized in the formation length is considered as an indication of how much of the wake energy is going to be converted into aerodynamic fluctuations. This analysis is directly associated with the conclusions of Zielinska [35], who described the relation between the amplitude and position of the maximum global modes with the Reynolds number. Two exponential laws are proposed:

$$C'_D = \alpha \exp\left(\beta \frac{L_f}{d}\right) \qquad C'_L = \alpha \exp\left(\beta \frac{L_f}{d}\right) \tag{9}$$

The evolution of the RMS drag and lift coefficients with the formation length are presented in Fig. 11 and 12, respectively. Once more, it was necessary to separate the two regimes when calculating the regression laws. For the RMS drag coefficient, points that represent flows in regime II are concentrated and biased the fit; for the lift, the behavior cannot be described solely by the formation length, since all the points corresponding to regime II flows are concentrated at $L_f \sim 0.6$.

Similar to what is presented on Section IV.A.1, points are scattered around the global models while geometry based laws fit well (Fig. 23 and 24). For the points at regime I, following coefficients were obtained: $\alpha = 0.234$ and $\beta = -2.050$ for the drag and $\alpha = 1.205$ and $\beta = -0.928$ for the lift. Note that the exponential decay is twice as large for the the drag.

The critical formation length that is associated with regime II can be derived from the presented results. Values considering each geometry, the average and the global model are listed on Table 3. This reinforces the conclusion

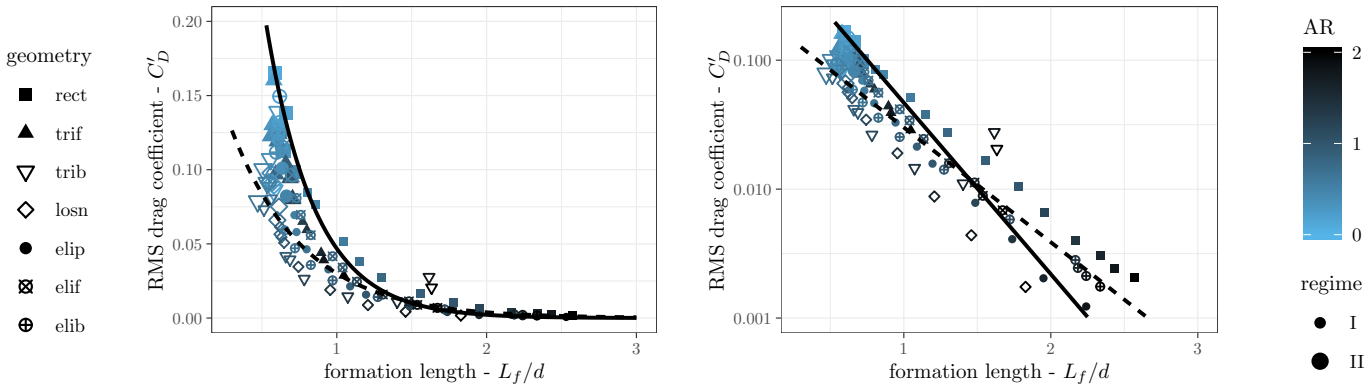

Fig. 11 Evolution of the RMS drag coefficient with the formation length, all geometries, colored by the aspect ratio (Re = 150)**; linear scale on the left and lin-log scale on the right. Represented regression laws: obtained for all points (solid line); only considering regime I (dashed line); and only considering regime II (dotted line).**

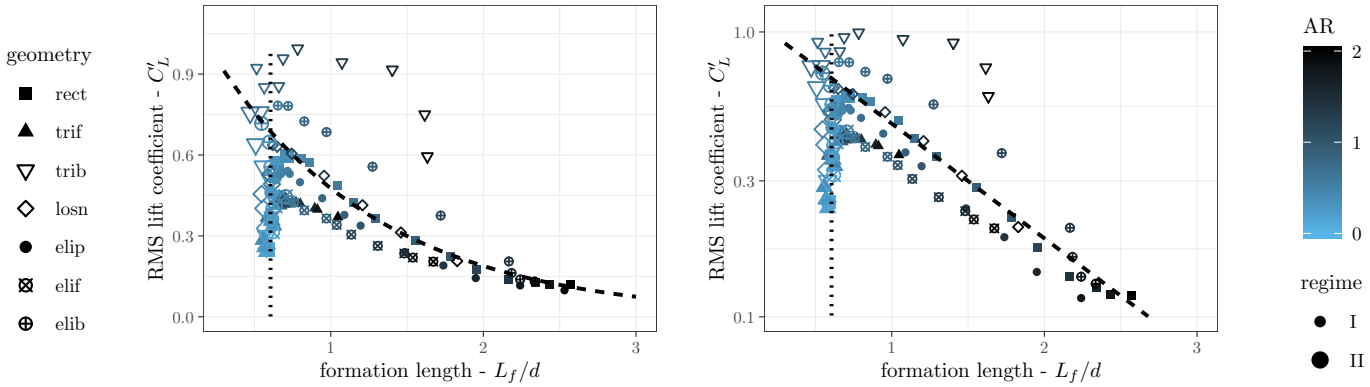

Fig. 12 Evolution of the RMS lift coefficient with the formation length, all geometries, colored by the aspect ratio (Re = 150)**; linear scale on the left and lin-log scale on the right. Represented regression laws: obtained for all points (solid line); only considering regime I (dashed line).**

that the second regime is associated with a saturation of the near-wake, being the value of $0.6d$ a limitation of the Von-Karman dynamics, believed to be a function of the Reynolds number.

Table 3 Critical formation length (L_f/d), Re = 150.

rect	trif	trib	losn	elip	elif	elib	**average**	all*
0.652	0.619	0.543	0.578	0.762	0.641	0.593	**0.605**	0.627

*: issued from the regressions performed for all geometries.

Although the discontinuity of the trends noted between the two regimes and the offset from the tendency curves being present for all geometries, that difference is more pronounced for the back-pointing shapes (trib and elib). That means that the mechanism of vortex shedding and its translation into force fluctuations is more affected by geometrical features placed further downstream of the body.

The proposed descriptions miss elements for the construction of solid models and further analysis is required, notable using multivariate analysis. Moreover, non-linearities can be noted, specially for the $C'_L(L_f/d)$ laws, but no simple model that captured that behavior could be found. However, obtained curves formalizes the link between the increase of the aerodynamic efforts and the decrease of the formation length (previously stated by Szepessy & Bearman [36], who associated more vigorous vortex shedding with a decrease of L_f) with two shape independent exponential laws.

The dispersion of the points for the RMS lift coefficient law can be explained by the fact that the formation length is a measure in the streamwise direction while the lift is by definition orthogonal to that. Based on this principle, a discussion based on observations in the y-direction is presented next.

3. RMS lift coefficient vs. vortex displacement

Visual examination of the vortex shedding lead to the observation that the amount of vertical displacement of the vortices from the surface of the body could be associated to the magnitude of the RMS lift coefficient, thus, to the aeolian tone. The quantification of that movement is performed with the analysis of the ω_z field contour, calculated using bi-linear interpolation.

For several timesteps that compose one period, the point in the iso-line $\omega_z = 0.1$ (value chosen arbitrarily) that is further from the body (biggest y) in the range $-b/2 \leq x \leq b/2$, defined as y_ω, is stored. For the complete vortex shedding cycle, the difference between the lowest and highest values of y_ω is defined as the flapping amplitude Δy_ω. The symmetry of the bodies allows for the measurement to be performed on the upper and lower sides and the mean value to be considered on the analysis.

Illustration of the lowest and highest points found in a cycle for different rectangular sections are presented in Fig. 13. As expected, the instantaneous point of max is at $x = b/2$. Tests were also performed using different range of streamwise coordinates (expanded shape and complete wake), but the obtained values were sparse and subjected to the difference of behavior in the wake, such as the two wake regimes, and were not directly associated to the fluctuations in the surface.

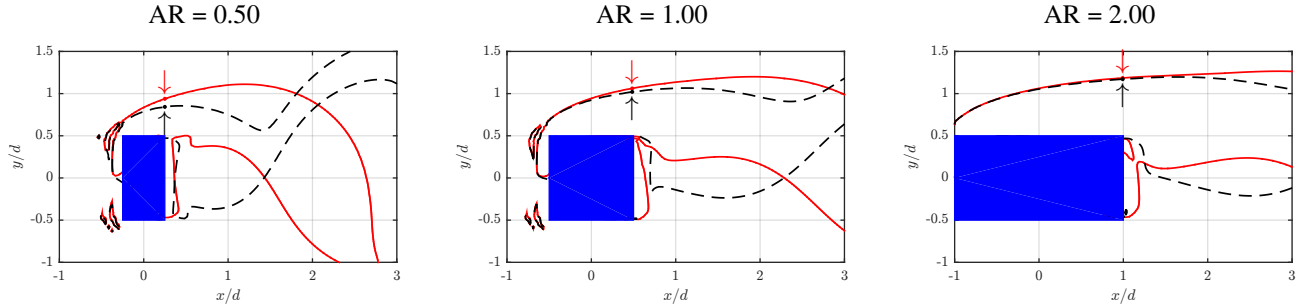

Fig. 13 Examples of the flapping quantification for rectangular section (rect) at Re = 150. Solid lines represent the iso-line corresponding to the timestep with maximum y_ω while dashed lines correspond to the flow that has minimum y_ω; arrows are directed to the points of minimal and maximal y_ω.

The correspondence between the 2 quantities is illustrated in Fig. 14. The relationship between the two variables is presented in Fig. 15. A least-squares fit is performed with an imposed crossing at (0,0).

$$C'_L = \alpha \Delta y_\omega \tag{10}$$

For all the points, the regression law is $C'_L = 4.3693\ \Delta y_\omega$ with an adjusted determination coefficient of 0.9282. It is notable that the points for the back-pointing triangle (trib) at small aspect ratio are out of the tendency. However, they do not impact the fit, that is found as $C'_L = 4.2825\ \Delta y_\omega$ when the points of trib are not considered. When each geometry is considered individually, the angular coefficient varies from 3.6 (trib) to 7.1 (elif).

Although it is possible that other curves represent better the trend noted in Fig. 15, the linear behavior is guarded due to the geometry-wise behavior, that is clearly linear (see Fig. 25). Nevertheless, similar relationships are also obtained when considering the average displacement y_ω (not shown), however the curves have discontinues associated to the two wake regimes.

The fact that the flapping of the vortex can be associated with the fluctuating lift, thus, the aeolian tone, is an important conclusion regarding the dynamics of the flow. Without any information about the shape or the flow regime

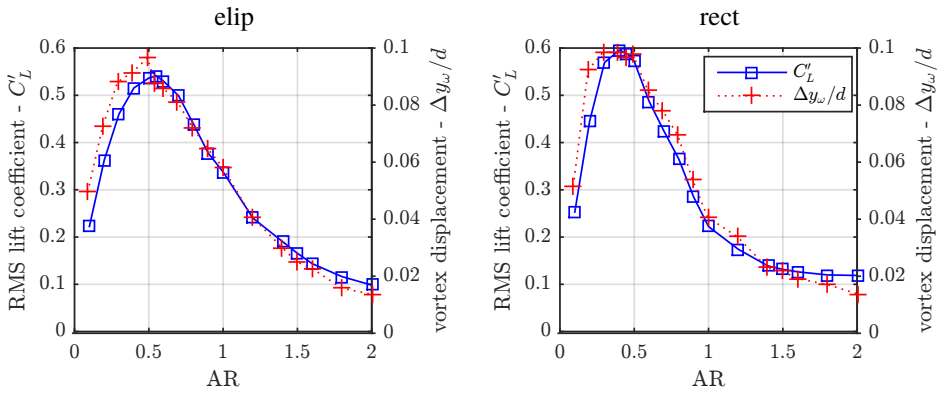

Fig. 14 Examples of the evolution of the RMS lift coefficient and vortex displacement with the aspect ratio for the elliptical sections (elip, left) and rectangular section (rect, right), Re **= 150.**

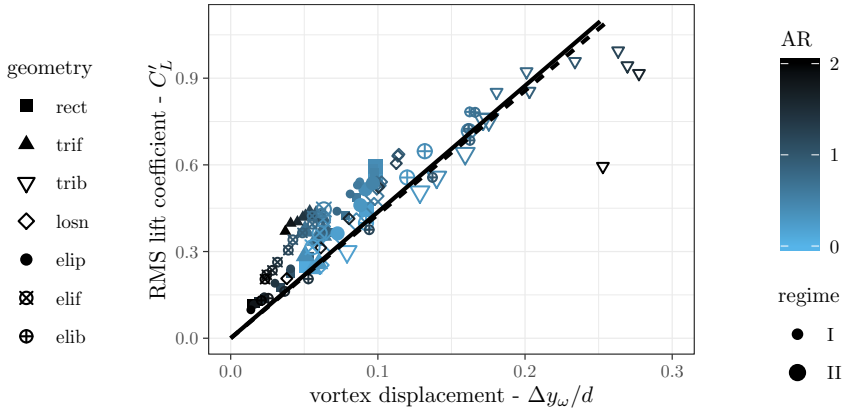

Fig. 15 Relationship between the RMS lift coefficient and the vortex displacement for all geometries colored by the aspect ratio, Re = 150**. Represented regression laws are obtained for all points (solid line) and without the back-pointing triangle, trib (dashed line).**

(model was also tested with results for the same geometries at different Reynolds number - lower than 150 - and the trend remained consistent), the access to the punctual movement can provide an estimation of the sound trait. A proper theoretical development to clarify and expand this empirical finding, notably based on the expression of surface force in terms of vorticity [37], is envisaged.

B. Integral quantities and geometry based relations

Relations based on the integral quantities are more interesting in an application point of view since they are more accessible than flow features, either by experiments or simulations. This section presents relationships that were found between the RMS force coefficients and the aspect ratio, the distance to the critical Reynolds number and the average drag coefficient.

1. RMS lift coefficient vs. aspect ratio

Model synthesis The evolution of the RMS lift coefficient presents, for all geometries, an initial increase followed by a decrease, as discussed in section III.A, and also noted for rectangular sections in previous works at both low [5, 38, 39] and high [40, 41] Reynolds numbers. Such biphasic response is largely discussed in biological sciences and is known as hormesis, defined by a low-dose stimulation and a high-dose inhibition [42]. The universality of such behavior in the response of the flow to an increase of the aspect ratio lead to the proposition of the following relationship:

$$\{C_L'\} = A\{\mathrm{AR}\}_{C_L'}^{B} \exp\left(\frac{\{\mathrm{AR}\}_{C_L'}}{C}\right) \tag{11}$$

where the operation represented by $\{\bullet\}_q$ is the normalization by the value corresponding to the maximum behavior (maximum q) for that given geometry and flow regime (Re), for example, $\{\mathrm{AR}\}_{C_L'}$ is the aspect ratio divided by the aspect ratio that corresponds to the maximum C_L' at that corresponding Reynolds number. Imposing the point $(\{\mathrm{AR}\}_{C_L'}, \{C_L'\}) = (1,1)$, that is by definition present for all the geometries and flow conditions, the following condition is obtained:

$$C = \frac{1}{-\log(A)} \tag{12}$$

thus, reducing the model to only 2 parameters: A, related to the magnitude of the curve and the exponential growth; and B, which represents the influence of the available surface to the resulting C_L'. This formulation is compatible with the considerations concerning the decrease of the surface pressure fluctuation with the increase of available surface (with the augmentation of the aspect ratio) presented by Inasawa [5].

The resulting equations are tested for different Reynolds numbers and are presented in Fig. 16. Results for regimes different from Re = 150 are issued from the procedure to estimate the critical Reynolds number [33], so are naturally less numerous. Also, due to the difference in Re_c, some geometries have null C_L' for some of the given Reynolds number and are naturally not presented. Curve coefficients are obtained from a least-squares linear regression and are presented on Table 4.

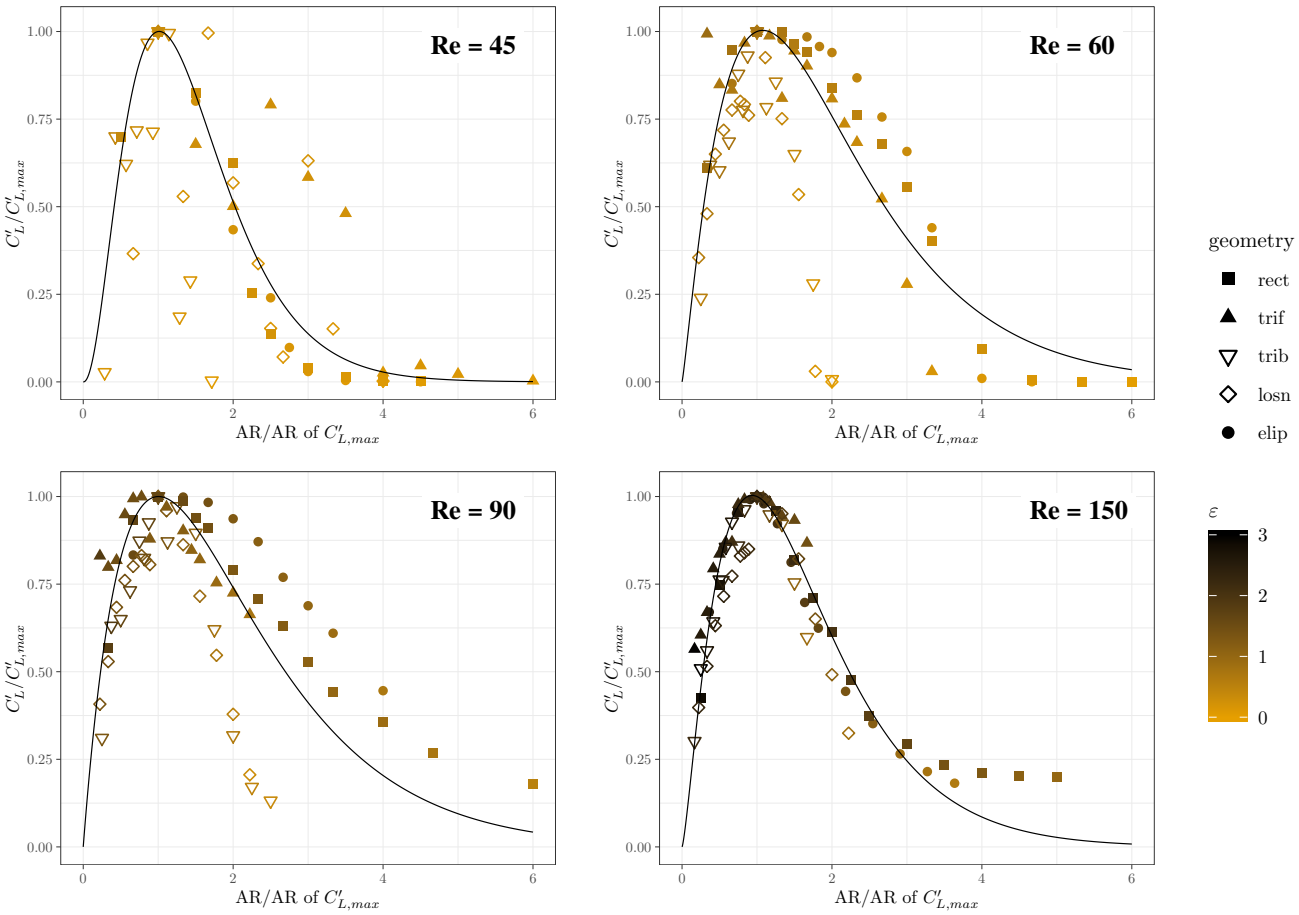

Fig. 16 Evolution of the RMS lift coefficient with the aspect ratio, both quantities normalized by the levels corresponding to the point of $\max(C_L')$**, multiple** Re**. Regression curves are as presented in Eq. (11)**

.

Figure 16 show that the relation is less geometry dependent with the increase of the Reynolds number. This can be directly associated also with the increase of the ε, that is, the farther from the transition, the less the geometry influences the wake if at a fixed Re. The asymptotic behavior is fully representative of all geometries for AR $\rightarrow$ 0 (null C'_L), however, for an increase of the aspect ratio the points deviate from the trend law. It is believed that this is due to the repositioning of detachment point for large bodies (see [43], for instance) for Re > 60, thus, changing into a different flow dynamics.

Table 4 Regression coefficients of the model of the normalized RMS lift coefficient as a function of the normalized aspect ratio, Eq. (11).

Re	45	60	90	150
A	9.3718	2.9877	2.6879	4.24700
B	2.2678	1.1798	0.9925	1.35423

While coefficient A is largely modified by the Re, B is, for Re > 45, more or less constant and fluctuates around 1. This confirms the distinction between the phenomena that compose the law: the scaling of the lift fluctuation is mainly defined by A and C, thus, it is intrinsically controlled by the incoming flow inertia to viscosity ratio, that can also be interpreted as the amount of incoming energy; on the other hand, the coefficient B, which represents the increase of available surface for the conversion of that wake energy into lift fluctuation, is barely untouched.

When reconstructing the original values of RMS lift coefficient and aspect ratio from the corresponding reference values, the following law is derived:

$$C'_L = \alpha \mathrm{AR}^{\beta} \exp\left(-\gamma \mathrm{AR}\right) \tag{13}$$

with:

$$\alpha = \frac{AC'_{L,max}}{\left(\mathrm{AR}|_{C'_L=C'_{L,max}}\right)^B}, \qquad \beta = B, \qquad \gamma = \frac{\log(A)}{\mathrm{AR}|_{C'_L=C'_{L,max}}} \tag{14}$$

The model can either be derived using the coefficients issued from the global regression coefficients A and B and Eq. (14) or calculating new fits for each geometry. Both approaches are performed and the results are listed on Table 5 for Re = 150. Regressions are performed for each geometry using the the model fitting function nls [44] in R [45]; the values of α, β and γ calculated using Eq. (14) are used as the starting values for the non-linear regression.

Table 5 Regression coefficients of the model of the RMS lift coefficient as a function of the aspect ratio, Re = 150 **- Eq. (13).**

geometry	$\mathrm{AR}\|_{C'_L=C'_{L,max}}$	$C'_{L,max}$	universal model*		individual model		
			α	γ	α	β	γ
elip	0.55	0.541	5.1644	1.1420	4.5207	1.2447	2.5548
losn	0.90	0.636	3.1171	0.6979	3.6152	1.6027	1.8299
rect	0.40	0.596	8.7540	1.5702	5.8863	1.1957	3.0869
trib	1.20	0.995	3.3002	0.5234	3.4555	1.4073	1.2965
trif	1.20	0.427	1.4155	0.5234	0.6986	0.6689	0.5331

*: coefficients derived from Eq. (14), $\beta = B = 1.3542$

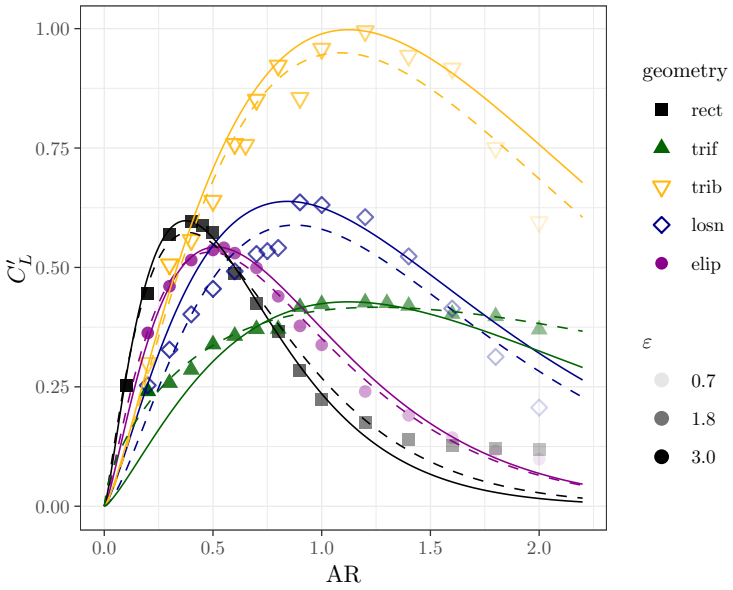

Fig. 17 Evolution of the RMS lift coefficient with the aspect ratio, Re = 150**. Continuous lines correspond to the model using $\beta = B$ (value issued from the regression of all the geometries), hatched line represents the non-linear regression of 3 parameters performed for each geometry.**

Physical insights allowed by the model Both regression models are presented in Fig. 17 and fit well the original values of C'_L(AR). While the magnitude α is the highest for the rectangular section, the decay is also the biggest, with $\gamma > 3$. Combination of the 2 events results in the rectangular section having its maximum C'_L for the shortest geometry. In the opposite direction is the front-pointing triangular section, which has small α and γ values. Similar of what is seen for the universal model, the scaling coefficients (α and γ) fluctuate more than the coefficient related to the length (β). Thus, while flow modification and change of the capabilities of the obstacle to respond to flow fluctuations cannot be easily separated, it seems that that the influence of the geometry to the production of RMS lift is more a matter of the modification of the strength of wake perturbations than the available surface for the generation of the lift.

The fact the β is not exactly 1 and not geometry independent (from 0.7 to 1.6) is an important conclusion in what concerns the geometrical efficiency. The extreme shapes (front-pointing triangle and lozenge) illustrate well the geometrical features that need to be favored when reducing the sound emission: the flow detachment has to be delayed and take place in regions where pressure fluctuations will not be able to result in lift fluctuations (for example in the form of a sharp edge at the end of the body). However, this statement cannot be considered individually, since this conclusions regards only the power component of the model. The fact that everything can be scaled differently due to a more or less energetic near-wake (coefficients α and γ) needs to be considered.

The combination of a blockage d and a breadth b defines the velocity gradient that is generated by the body, thus, the strength of the vortex. The geometrical details of the geometry (rectangular, triangular, etc), is mainly going to define how the wake is going to be organized, thus, where vortex shedding is going to take place and consequently the frequency and amplitude of the aerodynamic efforts. In that sense, the use of the Reynolds number based on the macro parameter d is fundamentally correct, once it determines the scale of the flow, however, the nuance of the geometry, the sole source of difference in the integral and topological results, is also a crucial parameter to be considered. One important conclusion that can be drawn from the given regression laws is the universality of the given analysis when considering the aspect ratio.

2. RMS force coefficients vs. distance to the critical Reynolds number

A relationship between the RMS force coefficients and the distance to the critical Reynolds number represented by the parameter ε is as well noted. The lift coefficient is normalized by the aspect ratio so bodies of different breadth are comparable. Following models are proposed:

$$\frac{C'_L}{\mathrm{AR}} = \alpha\varepsilon^{\beta} \qquad\qquad C'_D = \alpha\varepsilon^{\beta} \tag{15}$$

A polynomial model, based on the formula proposed by Norberg [31] is also considered:

$$\left(\frac{C'_L}{\mathrm{AR}}\right)^2 = \alpha\varepsilon + \beta\varepsilon^2 \tag{16}$$

In [31], $\alpha = 1/30 \approx 0.033$ and $\beta = 1/90 \approx 0.011$ for circular cylinder. Obtained curves are illustrated in Fig. 18, regression coefficients are presented on Table 6.

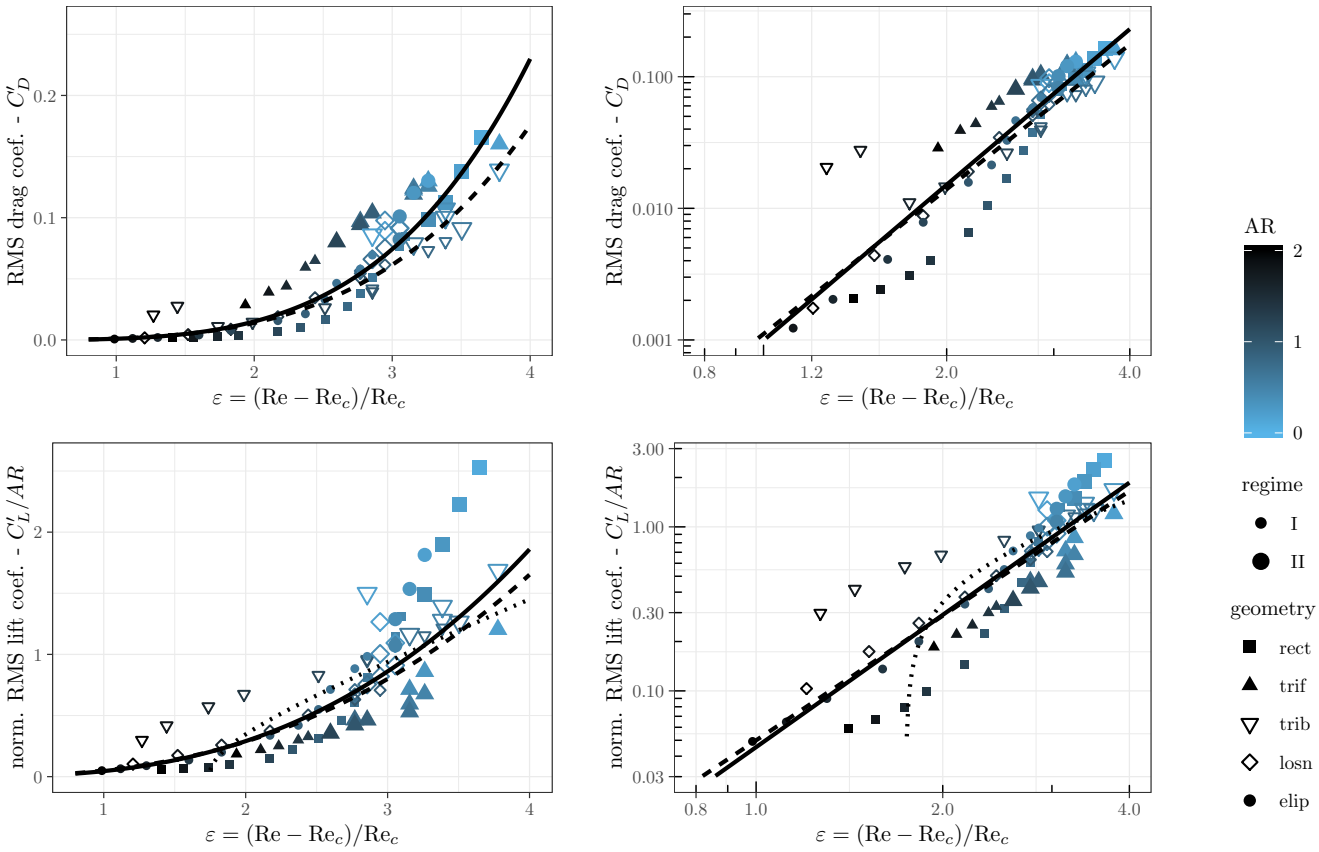

Fig. 18 Evolution of drag (top) and lift (bottom) RMS force coefficients with ε, linear (left) and log-log (right) scales. Represented regression laws: obtained for all points (solid line); only considering regime I (dashed line); and C'_L model based on the equation proposed by Norberg [31] (dotted lines) calculated for points at regime I.

Similar to what was obtained for previous discussed models ($C'_L(L_r/d)$, $C'_D(L_r/d)$ and $C'_D(L_f/d)$), there are some intrinsic deviations from the global laws while more consistent fits are obtained when every geometry is evaluated individually (see Fig. 26 and 27). Even though, the relation between the fluctuating efforts and ε is evidenced, and can also be taken as universal. The polynomial model is not very representative of a set of multiple geometries.

The rectangle and back-pointing triangle are the sections that deviate the most from the universal regression models. It can be argued that these deviations are associated with a shift in the mechanism of the generation of the fluctuating lift and drag for such kind of geometries for elongated bodies (AR > 1), that present flow reattachment.

The given laws naturally lead to the analysis of the ratio between the RMS lift and drag coefficients, illustrated in Fig. 19.

The dispersion of points in both graphs in Fig. 19 evidences the influences of the shape and the regime that are less notable in Fig. 18. The front-pointing triangle has the most continuous behavior, having an almost constant RMS lift-to-drag ratio, while the lozenge and back-pointing triangle range from 10 to 60.

Table 6 Regression coefficients for normalized RMS, Eq. (11).

		C'_L/AR		C'_D
		$\alpha\varepsilon^\beta$	$\sqrt{\alpha\varepsilon+\beta\varepsilon^2}$	$\alpha\varepsilon^\beta$
all points	α	0.0454	-0.89468	0.0010
	β	2.6783	0.43457	3.9275
regime I only	α	0.0500	-0.40649	0.0011
	β	2.5237	0.23319	3.6531

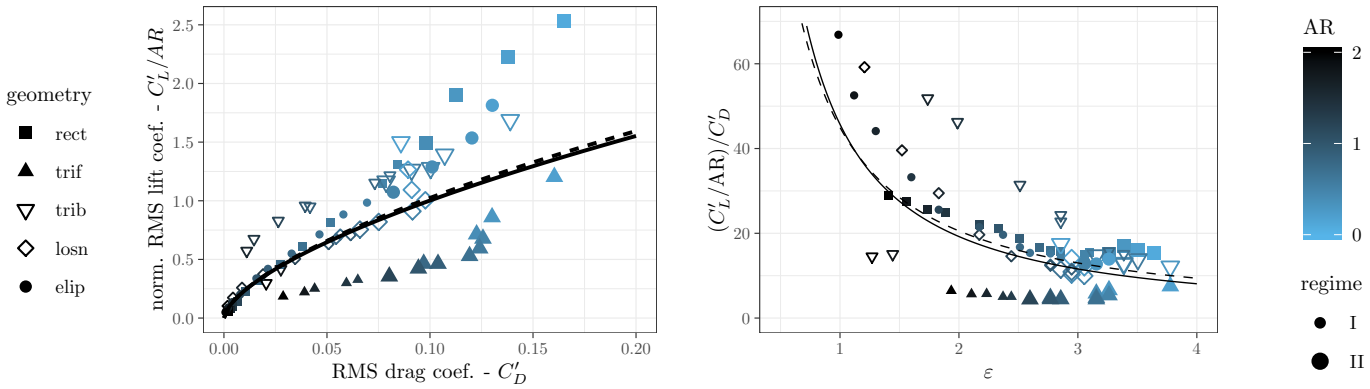

Fig. 19 Evolution of the normalized RMS lift coefficient with the RMS drag coefficient (left) and the evolution of the lift-to-drag RMS coefficients ratio with ε (right), Re = 150**. Represented regression laws: obtained for all points (solid line); and only considering regime I (dashed line).**

It can also be seem that the bigger ε, the more concentrated are the points, leading to the conclusion that the further from the transition there is less influence of the geometry on the levels of the fluctuating aerodynamic efforts and noise. This could be a biased interpretation due to the fact that large ε values in this work are associated with shorter geometries that are similar in terms of shape (all geometries are converging to a flat plate), thus, less discordance between the points is expected.

We may infer that both the drag and lift fluctuation coefficients and the relationship between them can be, partially, associated with the distance to the transition. Even though the points are scattered around the tendency curves, the importance of ε (or any other energy related parameter) as a fundamental ingredient for modeling the phenomenon is noted.

3. RMS lift coefficient vs. mean drag

Empirical laws relating noise and mean drag has been previously proposed by Revell et al. [46]. In an analogous manner, a power relationship between the RMS lift coefficient and the mean drag, Eq. (17), is found in this work. This analysis is only fruitful after normalizing the C'_L by the sectional breadth. This normalization transforms the value of fluctuating lift so it represents with more fidelity the pressure fluctuation on surface.

$$\frac{C'_L}{\mathrm{AR}} = \alpha|C_D|^\beta \tag{17}$$

Points and obtained regression laws considering the complete database and only flows at the regime I are presented in Fig. 20. Obtained coefficients are $\alpha = 0.0722$ and $\beta = 3.85740$, with adjusted determination coefficient of $R^2 = 0.8863$. When only regime I is considered, coefficients are $\alpha = 0.0661$ and $\beta = 4.210$, with adjusted $R^2 = 0.8819$.

This association may be justified from 2 different approaches. From an energetic point of view, we can link the drag

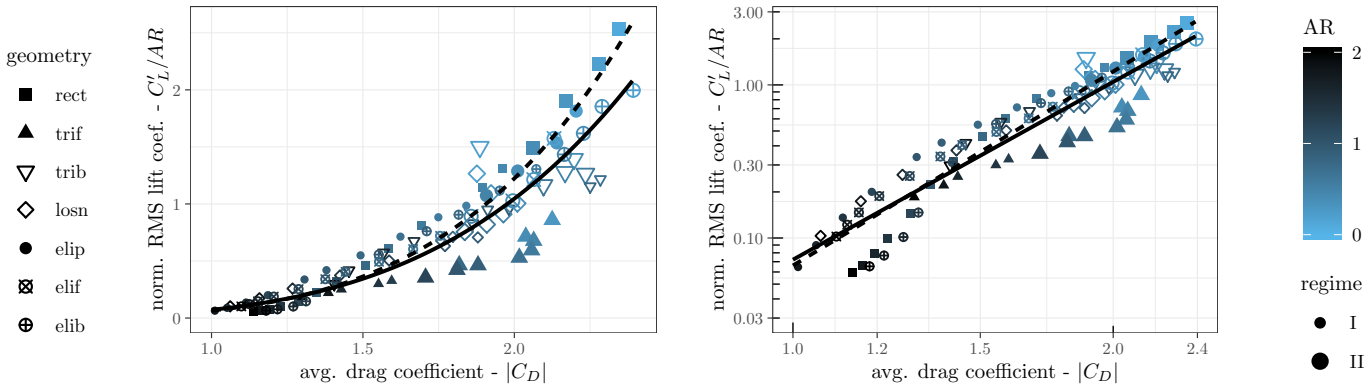

Fig. 20 Evolution of the normalized RMS lift coefficient with the average drag, Re = 150, all geometries, colored by the aspect ratio; linear scale on the left and log-log scale on the right. Represented regression laws: obtained for all points (solid line); and only considering regime I (dashed line).

coefficient to the amount of energy necessary to the cylinder to advance at the given speed in a fluid medium [47]. That energy is disposed at the wake, thus, we may associate a bigger drag to a more energetic wake, that consequently has a bigger pressure fluctuation at the obstacle's walls, thus, RMS lift coefficient and sound emission. From a wake topology perspective, an increase of average drag is in fact a decrease of the mean base pressure, that is related to an enhancement of the low-pressure vortices [48], thus, an increase of the RMS lift, the opposite of the effect of the splitter plate initially studied by Roshko [3].

For other Reynolds numbers, the relationship remains consistent, but the fit returns slightly different coefficients. Regression laws obtained using the values issued from the critical Reynolds determination study [33] are presented in Table 7. Since the unsteadiness is not present for all points, a threshold of $\varepsilon \geq 0.3$ is used; the regression for all Reynolds numbers considers both wake regimes.

Table 7 Regression coefficients of the model of the normalized RMS lift coefficient as a function of the average drag, Eq. (17).

Re	45*	60*	90*	150	all
$\log(\alpha)$	-5.156	-4.5493	-3.7275	-2.7166	-3.2311
α	0.0058	0.0106	0.0241	0.0661	0.0395
β	6.2490	6.0495	5.1770	4.2100	4.2616

*: for rect, trif, trib, losn and elip, $\varepsilon \geq 0.3$

For an increase of Re there is an increase of the coefficient α and decrease of exponent β. Naturally, the disparity between the two coefficients is believed to be due to modifications of the viscous dissipation ratio associated to the change of the Reynolds number. Further investigation must be performed in order to explain that behavior.

The analysis of laws derived independently for each geometry, Fig. 28, shows that the model underestimates the lift coefficient at the central drag values and overestimate at the extremities. Such behavior is a sign of non-linearities that are not captured by the proposed law. Considering the log-log scale, even though a polynomial model ($\alpha \log(|C_D|)^2 + \beta \log(|C_D|) + \gamma$) results in a better fit, the linear equation is chosen due to its simplicity and overall good representativeness of the relationship.

Recalling that this is an overall tendency, it does not imply that a shape that has a minimal drag will be the one with the smallest RMS lift, notable in the case of aspect ratios that are different than one, but proves that both phenomena (average drag and fluctuating lift) are related in at a given Reynolds number and will generally be reduced together, as noted in [18].

V. Concluding remarks

Flow around bluff bodies of different shapes and breadth-to-height ratios is studied in 2D, low Reynolds number (Re = 150) using a DNS solver. The flow is described in terms of integral quantities and wake topology. Based on a single formula aeroacoustic analogy, focus is given in the analysis of the RMS drag and lift coefficients. Several relations are discussed and summarized in Table 8.

Table 8 Summary of discussed models.

#	variables			section	equation
1	RMS lift coefficient	×	recirculation length	IV.A.1	$C'_L = \alpha + \beta\,(L_r/d)$
2	RMS drag coefficient	×	formation length	IV.A.2	$C'_D = \alpha + \exp(\beta\, L_f/d)$
3	RMS lift coefficient	×	formation length	IV.A.2	$C'_L = \alpha + \exp(\beta\, L_f/d)$
4	RMS lift coefficient	×	vortex vertical displacement	IV.A.3	$C'_L = \alpha\Delta y_\omega$
5	RMS lift coefficient	×	aspect ratio	IV.B.1	$C'_L = \alpha \mathrm{AR}^\beta \exp(-\gamma \mathrm{AR})$
6	RMS lift coefficient	×	"distance" to transition	IV.B.2	$C'_L/\mathrm{AR} = \alpha\varepsilon^\beta$
7	RMS drag coefficient	×	"distance" to transition	IV.B.2	$C'_D = \alpha\varepsilon^\beta$
8	RMS lift coefficient	×	mean drag	IV.B.3	$C'_L/\mathrm{AR} = \alpha[C_D]^\beta$

Two wake regimes (single and double row of vortices) exist, being the second one associated with low aspect ratio geometries. The transition between the two is marked by a peak of RMS lift (C'_L) and wake frequency (St). Accounting for that difference in topology is fundamental when proposing models that correlate the flow quantities.

It is found that the distance of average and unsteady flow phenomena from the body grows inversely to the RMS force coefficients, thus, aeolian tone levels. Inverse conclusion is obtained when considering the flapping of the vortices on the upper and lower faces of the obstacle (linearly proportional to C'_L). With the increase of the aspect ratio, a mix of contrary effects (increase of the available surface and decrease of the level of surface pressure fluctuation) generates an hormetic response that is found to be universal. When considering the distance from the onset of unsteadiness in the Reynolds number scale, represented by parameter ε, fluctuating efforts are growing with exponents 2.5 and 3.6. The increase of the mean drag coefficient is, on average, accompanied by an increase of the normalized RMS lift coefficient.

The disparity between the increase of the available surface for the establishment of lift fluctuations versus the decrease of proximity of the vortices and of the energy in the wake is the main difficulty when prospecting about the sound efficiency of a given body. Despite being important, the respect of a Reynolds number similitude is not sufficient and actually goes against the principle of placing the different obstacles at an equal energetic scale so that the influence of the geometry alone is analyzed when investigating the sound emission. Limiting to the results presented in this document, ε is considered a better criterion that can summarize those energetic effects, thus, without any knowledge about the shape, given an estimation of the RMS force coefficients and aeolian tone level, with an important drawback that the critical Reynolds number must be known.

Geometries that can be associated to lower levels of noise are those that are capable to dissipate energy before the wake, what is associated with longer recirculation and formation lengths and a low ε. Such aspect is achieved for all geometries when increasing the aspect ratio. When comparing the shapes at fixed AR, bodies of increased bluffness (that impose a larger distance of the two shear layers and at the same time have reduced available surface for the production of lift fluctuation after the flow detachment) are the ones that have a lower acoustic efficiency For the set of tested geometries, the most silent shapes are the front pointing triangle at low aspect ratio ($\mathrm{AR} < 0.7$) and the rectangular cylinder at big aspect ratios ($\mathrm{AR} \geq 0.7$).

The extrapolation of this results to high Reynolds number, particularly for aeroacoustics applications, is delicate. Cross-sectional shape has a fundamental role in the definition of the flow spanwise development, as investigated in [20, 49], so the use of current values and conclusions, limited to the 2D behavior, may not be directly transposed to an engineering context. Nonetheless, an intrinsic association between the sectional behavior and the spanwise organization is believed to exist. Authors recommend that further developments should be made in that direction of correlating both domains, especially in terms of instability analysis.

Appendix

A. Validation

In spite of the limited mesh resolution, the obtained values are similar to results reported on the literature, and trends generated by variations of both the geometry and the regime, as presented in Fig. 21, are well reproduced, the reader is invited to check [18, 19] for further discussion around the convergence of the used numerical setup.

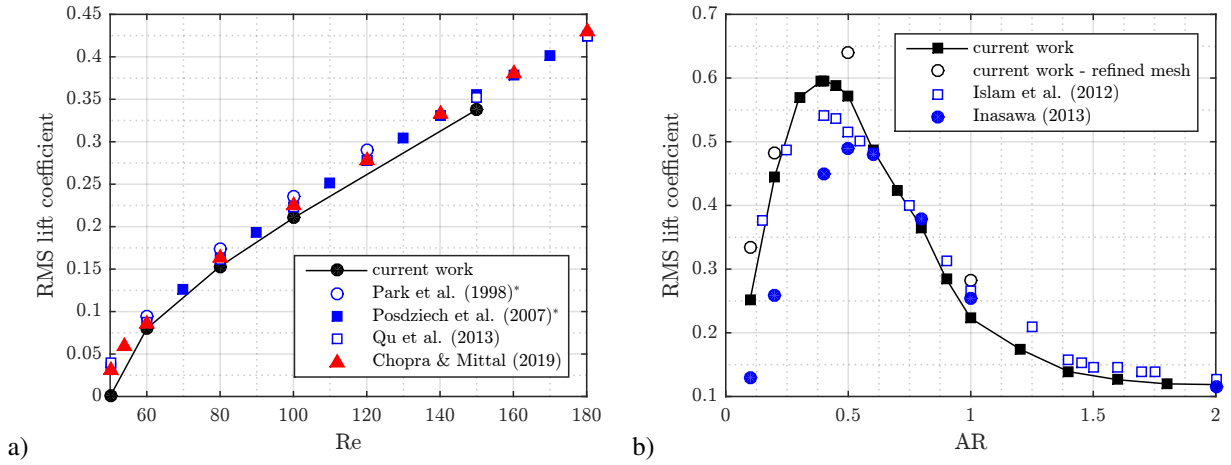

*: derived from the peak considering a sine wave - $C'_L = \max(C_L)/\sqrt{2}$

Fig. 21 Validation of the numerical setup: a) circular section at different regimes [27, 50–53]; and b): rectangular section at different AR, Re **= 150 [5, 38].**

B. Geometry based laws

The models coefficients and graphs on Section IV consider the full database. Since the different geometrical features under investigation may represent a change in the physical mechanism capable of spoiling the correlations the laws are tested for each group of geometries (same shape, multiple AR). The models calculated for each geometry individually are visually presented on this section. For conciseness, only the results for the rectangle, lozengle and ellipse (rect, losn and elip) are illustrated.

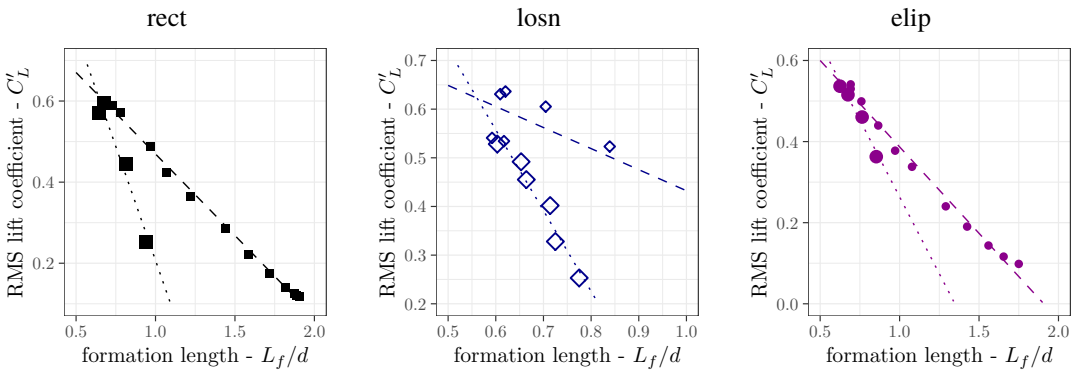

Fig. 22 Regression laws for the RMS lift coefficient as a function of the recirculation length (lin-lin scale); dashed line for regime I and dotted line for regime II.

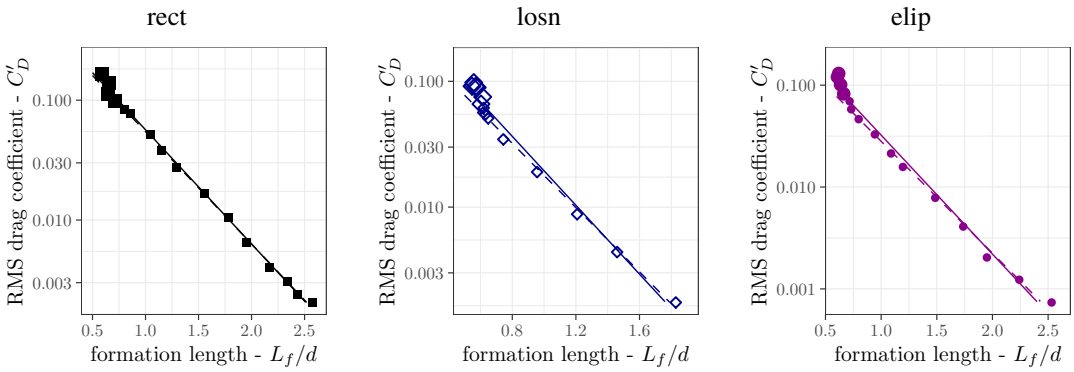

Fig. 23 Regression laws for the RMS drag coefficient as a function of the formation length (lin-log scale); dashed line for regime I and dotted line for regime II.

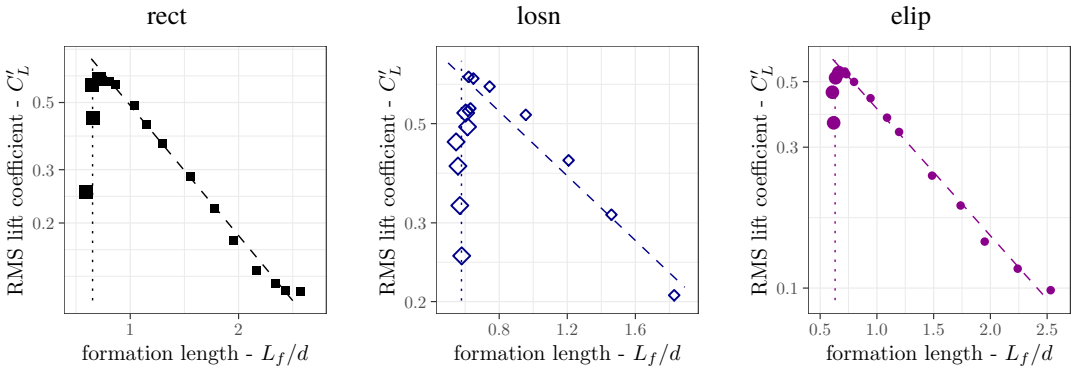

Fig. 24 Regression laws for the RMS lift coefficient as a function of the formation length (lin-log scale); dashed line for regime I and dotted line for regime II.

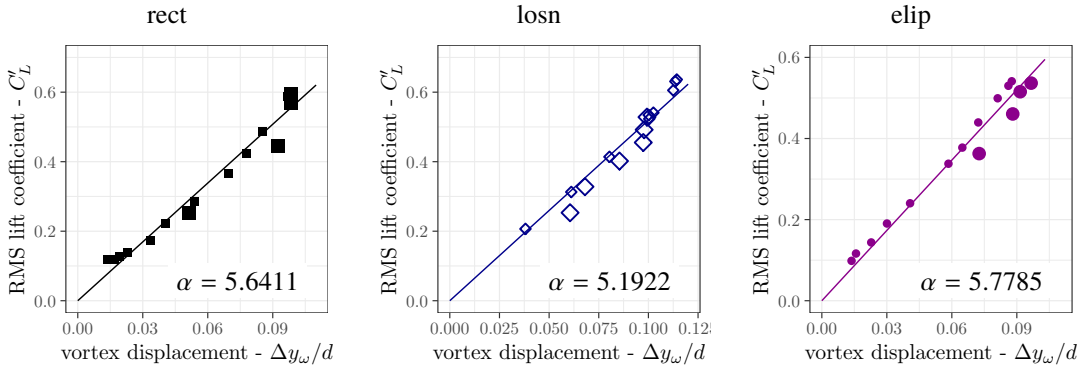

Fig. 25 Regression laws for the RMS lift coefficient as a function of the vortex vertical displacement Δy_ω (lin-lin scale).

Acknowledgments

The PhD funding of the first author was provided by the Ministére de l'Enseignement Supérieur et de la Recherche (MESR, french Ministry of Higher Education and Research), which is greatly appreciated.

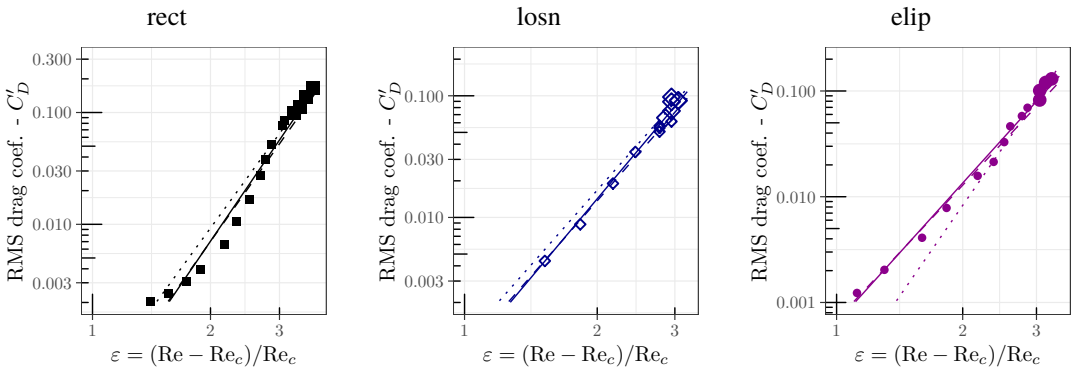

Fig. 26 Regression laws for the RMS drag coefficient as a function of ε (log-log scale); solid line for all points, dashed line for regime I and dotted line for regime II.

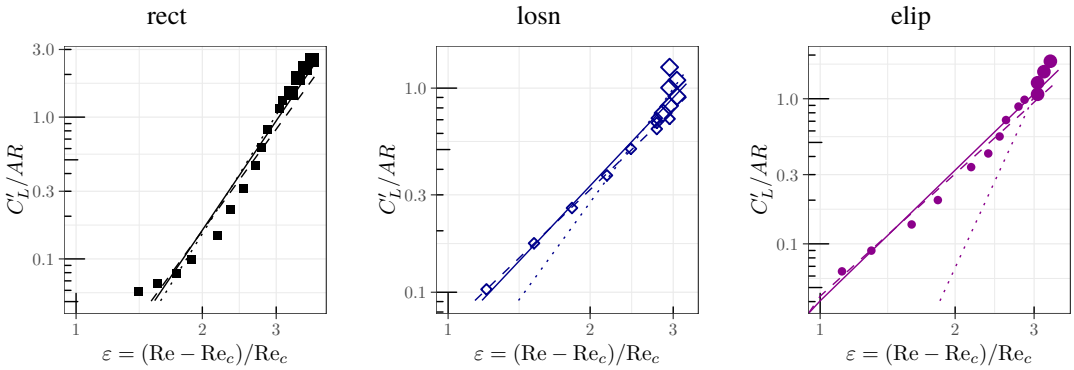

Fig. 27 Regression laws for the normalized RMS lift coefficient as a function of ε (log-log scale); solid line for all points, dashed line for regime I and dotted line for regime II.

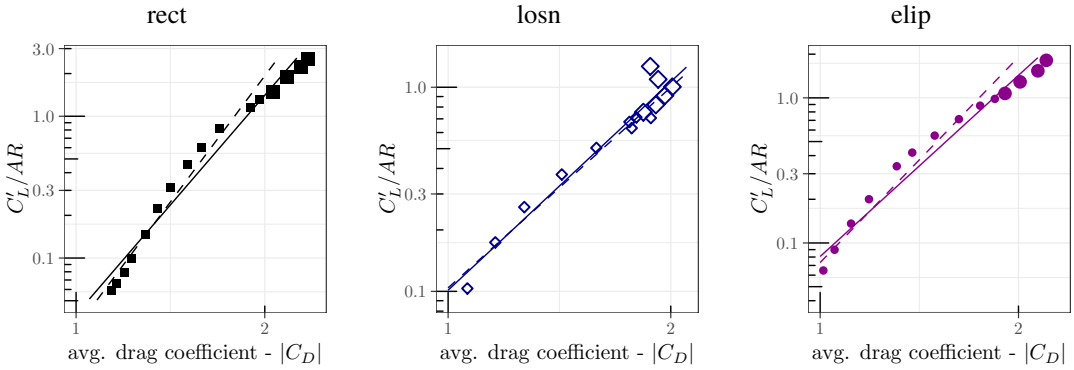

Fig. 28 Regression laws for the normalized RMS lift coefficient as a function of the average drag (log-log scale); solid line for all points and dashed line for regime I.

References

[1] Roshko, A., "Perspectives on bluff body aerodynamics," *Journal of Wind Engineering and Industrial Aerodynamics*, Vol. 49, No. 1, 1993, pp. 79 – 100. doi:https://doi.org/10.1016/0167-6105(93)90007-B, URL `http://www.sciencedirect.com/science/article/pii/016761059390007B`.

[2] Roshko, A., "On the drag and shedding frequency of two-dimensional bluff bodies," Tech. rep., National Advisory Committee

for Aeronautics, 1954.

[3] Roshko, A., "On the Wake and Drag of Bluff Bodies," *Journal of the Aeronautical Sciences*, Vol. 22, No. 2, 1955, pp. 124–132. doi:10.2514/8.3286, URL https://doi.org/10.2514/8.3286.

[4] Cheng, M., and Liu, G., "Effects of afterbody shape on flow around prismatic cylinders," *Journal of Wind Engineering and Industrial Aerodynamics*, Vol. 84, No. 2, 2000, pp. 181 – 196. doi:https://doi.org/10.1016/S0167-6105(99)00050-1, URL http://www.sciencedirect.com/science/article/pii/S0167610599000501.

[5] Inasawa, A., Asai, M., and Nakano, T., "Sound generation in the flow behind a rectangular cylinder of various aspect ratios at low Mach numbers," *Computers & Fluids*, Vol. 82, No. Supplement C, 2013, pp. 148 – 157. doi:https://doi.org/10.1016/j.compfluid.2013.05.006, URL http://www.sciencedirect.com/science/article/pii/S0045793013001928.

[6] Margnat, F., "Hybrid prediction of the aerodynamic noise radiated by a rectangular cylinder at incidence," *Computers & Fluids*, Vol. 109, 2015, pp. 13 – 26. doi:http://dx.doi.org/10.1016/j.compfluid.2014.12.006, URL http://www.sciencedirect.com/science/article/pii/S0045793014004691.

[7] Luo, S., Yazdani, M., Chew, Y., and Lee, T., "Effects of incidence and afterbody shape on flow past bluff cylinders," *Journal of Wind Engineering and Industrial Aerodynamics*, Vol. 53, No. 3, 1994, pp. 375 – 399. doi:https://doi.org/10.1016/0167-6105(94)90092-2, URL http://www.sciencedirect.com/science/article/pii/0167610594900922.

[8] Hu, J. C., and Zhou, Y., "Aerodynamic Characteristics of Asymmetric Bluff Bodies," *Journal of Fluids Engineering*, Vol. 131, No. 1, 2008, pp. 011206–011206–9. doi:10.1115/1.2979229, URL http://dx.doi.org/10.1115/1.2979229.

[9] Becker, S., Hahn, C., Kaltenbacher, M., and Lerch, R., "Flow-Induced Sound of Wall-Mounted Cylinders with Different Geometries," *AIAA Journal*, Vol. 46, No. 9, 2008, pp. 2265–2281. doi:10.2514/1.34865, URL https://doi.org/10.2514/1.34865.

[10] King, F., and Pfizenmaier, E., "An experimental study of sound generated by flows around cylinders of different cross-section," *Journal of Sound and Vibration*, Vol. 328, No. 3, 2009, pp. 318 – 337. doi:https://doi.org/10.1016/j.jsv.2009.07.034, URL http://www.sciencedirect.com/science/article/pii/S0022460X09006221.

[11] Iglesias, E. L., Thompson, D., and Smith, M., "Experimental study of the aerodynamic noise radiated by cylinders with different cross-sections and yaw angles," *Journal of Sound and Vibration*, Vol. 361, 2016, pp. 108 – 129. doi:https://doi.org/10.1016/j.jsv.2015.09.044, URL http://www.sciencedirect.com/science/article/pii/S0022460X15007841.

[12] Curle, N., "The influence of solid boundaries upon aerodynamic sound," *Proceedings of the Royal Society of London A: Mathematical, Physical and Engineering Sciences*, Vol. 231, No. 1187, 1955, pp. 505–514. doi:10.1098/rspa.1955.0191, URL http://rspa.royalsocietypublishing.org/content/231/1187/505.

[13] Phillips, O. M., "The intensity of Aeolian tones," *Journal of Fluid Mechanics*, Vol. 1, No. 6, 1956, p. 607–624. doi:10.1017/S0022112056000408.

[14] Fujita, H., "The characteristics of the Aeolian tone radiated from two-dimensional cylinders," *Fluid Dynamics Research*, Vol. 42, No. 1, 2010, p. 015002. URL http://stacks.iop.org/1873-7005/42/i=1/a=015002.

[15] Lighthill, M. J., "On sound generated aerodynamically I. General theory," *Proceedings of the Royal Society of London A: Mathematical, Physical and Engineering Sciences*, Vol. 211, No. 1107, 1952, pp. 564–587. doi:10.1098/rspa.1952.0060, URL http://rspa.royalsocietypublishing.org/content/211/1107/564.

[16] Laizet, S., and Lamballais, E., "High-order compact schemes for incompressible flows: A simple and efficient method with quasi-spectral accuracy," *Journal of Computational Physics*, Vol. 228, No. 16, 2009, pp. 5989 – 6015. doi:https://doi.org/10.1016/j.jcp.2009.05.010, URL http://www.sciencedirect.com/science/article/pii/S0021999109002587.

[17] Margnat, F., and Morinière, V., "Behavior of an immersed boundary method in unsteady flows over sharp-edged bodies," *Computers and Fluids*, Vol. 38, No. 6, 2009, pp. 1065–1079.

[18] Pinto, W. J. G. S., and Margnat, F., "Shape optimisation for the noise induced by the flow over compact bluff bodies," *International Conference on Computational Fluid Dynamics (ICCFD10), July 9th-13th, Barcelona, Spain*, 2018.

[19] da Silva Pinto, W. J. G., and Margnat, F., "A shape optimization procedure for cylinders aeolian tone," *Computers & Fluids*, Vol. 182, 2019, pp. 37 – 51. doi:https://doi.org/10.1016/j.compfluid.2019.02.002, URL http://www.sciencedirect.com/science/article/pii/S0045793019300283.

[20] Pinto, W. J. G. S., Margnat, F., and Gervais, Y., "Effect of cross-section on flow three-dimensionality for prismatic bodies and the associated noise emission," *25th AIAA/CEAS Aeroacoustics Conference (Aeroacoustics 2019), 20-24 May, Delft, The Netherlands*, 2019.

[21] Fage, A., Johansen, F. C., and Lamb, H., "On the flow of air behind an inclined flat plate of infinite span," *Proceedings of the Royal Society of London. Series A, Containing Papers of a Mathematical and Physical Character*, Vol. 116, No. 773, 1927, pp. 170–197. doi:10.1098/rspa.1927.0130, URL https://royalsocietypublishing.org/doi/abs/10.1098/rspa.1927.0130.

[22] Johnson, S. A., Thompson, M. C., and Hourigan, K., "Predicted low frequency structures in the wake of elliptical cylinders," *European Journal of Mechanics - B/Fluids*, Vol. 23, No. 1, 2004, pp. 229 – 239. doi:https://doi.org/10.1016/j.euromechflu.2003.05.006, URL http://www.sciencedirect.com/science/article/pii/S0997754603001055, bluff Body Wakes and Vortex-Induced Vibrations.

[23] Thompson, M. C., Radi, A., Rao, A., Sheridan, J., and Hourigan, K., "Low-Reynolds-number wakes of elliptical cylinders: from the circular cylinder to the normal flat plate," *Journal of Fluid Mechanics*, Vol. 751, 2014, p. 570–600. doi:10.1017/jfm.2014.314.

[24] Saha, A. K., "Far-wake characteristics of two-dimensional flow past a normal flat plate," *Physics of Fluids*, Vol. 19, No. 12, 2007, p. 128110. doi:10.1063/1.2825413, URL https://doi.org/10.1063/1.2825413.

[25] Ng, Z. Y., Vo, T., Hussam, W. K., and Sheard, G. J., "Two-dimensional wake dynamics behind cylinders with triangular cross-section under incidence angle variation," *Journal of Fluids and Structures*, Vol. 63, 2016, pp. 302 – 324. doi:https://doi.org/10.1016/j.jfluidstructs.2016.04.003, URL http://www.sciencedirect.com/science/article/pii/S0889974615300293.

[26] Mahato, B., Ganta, N., and Bhumkar, Y. G., "Direct simulation of sound generation by a two-dimensional flow past a wedge," *Physics of Fluids*, Vol. 30, No. 9, 2018, p. 096101. doi:10.1063/1.5039953, URL https://doi.org/10.1063/1.5039953.

[27] Chopra, G., and Mittal, S., "Drag coefficient and formation length at the onset of vortex shedding," *Physics of Fluids*, Vol. 31, No. 1, 2019, p. 013601. doi:10.1063/1.5075610, URL https://doi.org/10.1063/1.5075610.

[28] Pier, B., "On the frequency selection of finite-amplitude vortex shedding in the cylinder wake," *Journal of Fluid Mechanics*, Vol. 458, 2002, p. 407–417. doi:10.1017/S0022112002008054.

[29] Norberg, C., "Fluctuating lift on a circular cylinder: review and new measurements," *Journal of Fluids and Structures*, Vol. 17, No. 1, 2003, pp. 57 – 96. doi:https://doi.org/10.1016/S0889-9746(02)00099-3, URL http://www.sciencedirect.com/science/article/pii/S0889974602000993.

[30] Schumm, M., Berger, E., and Monkewitz, P. A., "Self-excited oscillations in the wake of two-dimensional bluff bodies and their control," *Journal of Fluid Mechanics*, Vol. 271, 1994, p. 17–53. doi:10.1017/S0022112094001679.

[31] Norberg, C., "Flow around a circular cylinder: aspects of fluctuating lift," *Journal of Fluids and Structures*, Vol. 15, No. 3, 2001, pp. 459 – 469. doi:https://doi.org/10.1006/jfls.2000.0367, URL http://www.sciencedirect.com/science/article/pii/S0889974600903670.

[32] Ng, Z. Y., Vo, T., and Sheard, G. J., "Stability of the wakes of cylinders with triangular cross-sections," *Journal of Fluid Mechanics*, Vol. 844, 2018, p. 721–745. doi:10.1017/jfm.2018.161.

[33] Pinto, W. J. G. S., and Margnat, F., "Influence of bluff body sectional breadth and shape on the onset of flow unsteadiness," *submitted to Physics of Fluids*, 2019.

[34] Sheard, G. J., Fitzgerald, M. J., and Ryan, K., "Cylinders with square cross-section: wake instabilities with incidence angle variation," *Journal of Fluid Mechanics*, Vol. 630, 2009, p. 43–69. doi:10.1017/S0022112009006879.

[35] Zielinska, B. J. A., and Wesfreid, J. E., "On the spatial structure of global modes in wake flow," *Physics of Fluids*, Vol. 7, No. 6, 1995, pp. 1418–1424. doi:10.1063/1.868529, URL https://doi.org/10.1063/1.868529.

[36] Szepessy, S., and Bearman, P. W., "Aspect ratio and end plate effects on vortex shedding from a circular cylinder," *Journal of Fluid Mechanics*, Vol. 234, 1992, p. 191–217. doi:10.1017/S0022112092000752.

[37] Howe, M. S., *Theory of Vortex Sound*, Cambridge Texts in Applied Mathematics, Cambridge University Press, 2002, Chap. 4, p. 82–113. doi:10.1017/CBO9780511755491.

[38] Islam, S. U., Zhou, C. Y., Shah, A., and Xie, P., "Numerical simulation of flow past rectangular cylinders with different aspect ratios using the incompressible lattice Boltzmann method," *Journal of Mechanical Science and Technology*, Vol. 26, No. 4, 2012, pp. 1027–1041. doi:10.1007/s12206-012-0328-4, URL https://doi.org/10.1007/s12206-012-0328-4.

[39] Sohankar, A., Norberg, C., and Davidson, L., "A numerical Study of Unsteady Two-Dimensional Flow Around Rectangular Cylinders at Incidence," Tech. Rep. Internal Report Nr. 96/25, Departement of Thermo and Fluid Dynamics, Chalmers University of Technology, 1996.

[40] Sakamoto, H., Haniu, H., and Kobayashi, Y., "Fluctuating Forces Acting on Rectangular Cylinders in Uniform Flow : On Rectangular Cylinders with Fully Separated Flow (in japanese)," *Transactions of the Japan Society of Mechanical Engineers Series B*, Vol. 55, No. 516, 1989, pp. 2310–2317. doi:10.1299/kikaib.55.2310.

[41] Sohankar, A., "Large eddy simulation of flow past rectangular-section cylinders: Side ratio effects," *Journal of Wind Engineering and Industrial Aerodynamics*, Vol. 96, No. 5, 2008, pp. 640 – 655. doi:https://doi.org/10.1016/j.jweia.2008.02.009, URL http://www.sciencedirect.com/science/article/pii/S0167610508000238.

[42] Calabrese, E. J., and Baldwin, L. A., "Defining hormesis," *Human & Experimental Toxicology*, Vol. 21, No. 2, 2002, pp. 91–97. doi:10.1191/0960327102ht217oa, URL https://doi.org/10.1191/0960327102ht217oa, pMID: 12102503.

[43] Okajima, A., Nagahisa, T., and Rokugoh, A., "A Numerical Analysis of Flow around Rectangular Cylinders," *JSME international journal. Ser. 2, Fluids engineering, heat transfer, power, combustion, thermophysical properties*, Vol. 33, No. 4, 1990, pp. 702–711. doi:10.1299/jsmeb1988.33.4_702.

[44] Bates, D. M., and Chambers, J. M., "Nonlinear Models," *Statistical Models in S*, Wadsworth & Brooks/Cole, 1992.

[45] R Core Team, *R: A Language and Environment for Statistical Computing*, R Foundation for Statistical Computing, Vienna, Austria, 2017. URL https://www.R-project.org/.

[46] Revell, J. D., Prydz, R. A., and Hays, A. P., "Experimental Study of Aerodynamic Noise vs Drag Relationships for Circular Cylinders," *AIAA Journal*, Vol. 16, No. 9, 1978, pp. 889–897. doi:10.2514/3.60982, URL https://doi.org/10.2514/3.60982.

[47] Ahlborn, B., Seto, M. L., and Noack, B. R., "On drag, Strouhal number and vortex-street structure," *Fluid Dynamics Research*, Vol. 30, No. 6, 2002, pp. 379 – 399. doi:https://doi.org/10.1016/S0169-5983(02)00062-X, URL http://www.sciencedirect.com/science/article/pii/S016959830200062X.

[48] Darekar, R. M., and Sherwin, S. J., "Flow past a square-section cylinder with a wavy stagnation face," *Journal of Fluid Mechanics*, Vol. 426, 2001, p. 263–295. doi:10.1017/S0022112000002299.

[49] Pinto, W. J. G. S., and Margnat, F., "Experimental study of the influence of cross section shape on spanwise coherence length in flow around cylinders," *under consideration for publication*, 2019.

[50] Park, J., Kwon, K., and Choi, H., "Numerical solutions of flow past a circular cylinder at Reynolds numbers up to 160," *KSME International Journal*, Vol. 12, No. 6, 1998, pp. 1200–1205. doi:10.1007/BF02942594, URL https://doi.org/10.1007/BF02942594.

[51] Posdziech, O., and Grundmann, R., "A systematic approach to the numerical calculation of fundamental quantities of the two-dimensional flow over a circular cylinder," *Journal of Fluids and Structures*, Vol. 23, No. 3, 2007, pp. 479 – 499. doi:https://doi.org/10.1016/j.jfluidstructs.2006.09.004, URL http://www.sciencedirect.com/science/article/pii/S0889974606001083.

[52] Konstantinidis, E., and Bouris, D., "Bluff Body Aerodynamics and Wake Control," *Applied Aerodynamics*, edited by J. C. Lerner and U. Boldes, IntechOpen, Rijeka, 2012, Chap. 4. doi:10.5772/38684, URL https://doi.org/10.5772/38684.

[53] Qu, L., Norberg, C., Davidson, L., Peng, S.-H., and Wang, F., "Quantitative numerical analysis of flow past a circular cylinder at Reynolds number between 50 and 200," *Journal of Fluids and Structures*, Vol. 39, No. Supplement C, 2013, pp. 347 – 370. doi:https://doi.org/10.1016/j.jfluidstructs.2013.02.007, URL http://www.sciencedirect.com/science/article/pii/S0889974613000388.